AN ABSTRACT OF THE THESIS OF

Daniel M. Hess for the degree of Master of Science in Civil Engineering presented on June 2, 2016.

Title: Evaluation of Topography and Seismicity on Shallow Landslide Susceptibility

Abstract approved:

Ben A. Leshchinsky

Shallow landslides are a prevalent concern in mountainous regions that can result in severe societal, economic, and environmental impacts. The challenge is further compounded as the size and location of a potential slide is often unknown. This study presents a generalized approach for the evaluation of shallow landslide susceptibility using an existing shallow landslide inventory, remote sensing data, and various geotechnical scenarios. The three-dimensional limit equilibrium model uses a grid-based approach and uniquely incorporates tree root-reinforcement, earth pressure boundary forces, and pseudo-static seismic accelerations. Findings from this study include the back-calculation of soil strength from a landslide inventory, a convergence upon critical landslide size, and the determination of shallow landslide susceptibility for a landscape or infrastructure considering various root, water, and seismic conditions.

Evaluation of Topography and Seismicity on Shallow Landslide Susceptibility

by
Daniel M. Hess

A THESIS

submitted to

Oregon State University

in partial fulfillment of
the requirements for the
degree of

Master of Science

Presented June 2, 2016
Commencement June 2017

Master of Science thesis of Daniel M. Hess presented on June 2, 2016.

APPROVED:

Major Professor, representing Civil Engineering

Head of the School of Civil and Construction Engineering

Dean of the Graduate School

I understand that my thesis will become part of the permanent collection of Oregon State University libraries. My Signature below authorizes release of my thesis to any reader upon request.

Daniel M. Hess, Author

ACKNOWLEDGEMENTS

This thesis would not have been possible without help and support from several individuals. I would like to express my sincere appreciation to my advisor Dr. Ben Leshchinsky for guiding and mentoring me through this process, in addition to the many hours that he committed ensuring successful completion of this research. I would also like to thank Michael Bunn for all of his help implementing this study with numerous software programs and for his dedication to continue this research after I graduate. Thanks to Dr. Michael Olsen, Dr. Ben Mason, and Dr. Robert Kennedy for serving on my committee and providing valuable advice that helped shape this work. I am further grateful to the other faculty, staff, and students within the School of Civil and Construction Engineering for all of their knowledge and support during the past two years. Finally, I am indebted to my girlfriend Melissa, my parents Ken and Jan, and my sister Kristen for the endless supply of love and encouragement throughout my education.

CONTRIBUTION OF AUTHORS

Dr. Ben Leshchinsky was the principal investigator for this research. Michael Bunn's work as a graduate student consisted of ideas, some coding during analysis, and editing, while Dr. Michael Olsen and Dr. H. Benjamin Mason provided guidance that helped shape the direction of this study.

TABLE OF CONTENTS

Page

General Introduction 1

Evaluation of Topography and Seismicity on Shallow Landslide Susceptibility: A Simplified Three-Dimensional Slope Stability Framework 2

Abstract 2

Introduction 2

Methodology 5

Derivation of the Three-Dimensional Topographic Limit Equilibrium Model (3DTLE) 5

Lateral Earth Pressure 9

Application of 3DTLE Model 11

Geospatial Data 11

Soil and Root Properties 12

Analysis of Landslide Size and Shape 13

Susceptibility Analysis 14

Seismic Analysis 16

Overview of Analyses 18

Results and Discussion 19

Landslide Size and Shape 19

Susceptibility Analysis 20

Seismic Analysis 21

Comparison to Conventional Infinite Slope Analyses 22

Considerations for Applying 3DTLE 23

TABLE OF CONTENTS (Continued)

Page

Conclusion 26

Figures 28

Tables 40

Concluding Remarks 41

References 42

LIST OF FIGURES

Figure Page

1. (a) Isometric and (b) profile views of the proposed soil block with associated dimensions and forces. 28

2. Example of concave topography with the two side pixels at higher elevations than the center pixel. The shown boundary forces are due to lateral earth pressure. 29

3. Shaded relief map of a portion of the Gales Creek quadrangle showing the limits of the selected DEMs and considered shallow landslide deposits. The smaller DEM is used in the seismic analysis. 29

4. Mean back-calculated friction angle for changing values of water height ratio and root cohesion. 30

5. EW and NS acceleration-time series for the full-length scaled ground motions (left) and pseudo-spectral response with the design target spectrum (right) of two selected motions used in the scaling of 46 input motions. 30

6. Flow chart of the presented framework for analyzing shallow landslides. 31

7. Analysis of landslide shape. (a) An example of fitting rectangles to landslide deposit polygons, and (b) the ratio of rectangular dimensions are depicted as probabilities of occurrence. 32

8. The dependence of failure on pixel size for changing values of (a) root cohesion, (b) water height ratio, and (c) horizontal seismic coefficient. Baseline conditions used for non-changing parameters. 32

9. Distributions of (a) back-calculated friction angles for baseline conditions and (b) landslide depths obtained from the shallow landslide inventory. 33

10. Landslide susceptibility maps of Gales Creek, OR calculated using a product distribution and various input values of horizontal seismic coefficient and water height ratio. Root cohesion was held constant at 0 kPa for all four maps. 34

11. Comparison of the mean probability of failure calculated for various input values of horizontal seismic coefficient, water height ratio, and root cohesion. 35

LIST OF FIGURES (Continued)

Figure Page

12. Susceptibility map for Gales Creek watershed showing the probability of failure for four cases of horizontal seismic coefficient, water height ratio, and root cohesion overlaid on shaded relief. 36

13. Infrastructure risk maps for various cases of horizontal seismic coefficient, water height ratio, and root cohesion overlaid on shaded relief maps within the Gales Creek watershed. 37

14. Cumulative area of failure obtained by applying the shorter length motions to a smaller DEM tile near Gales Creek, OR. Four different combination of water height ratio and root cohesion were analyzed. 38

15. Difference in failure probability between the infinite slope model and the 3DTLE model for several cases. A positive difference signifies that the infinite slope model calculated a higher probability of failure, while a negative difference means 3DTLE. 39

Evaluation of Topography and Seismicity on Shallow Landslide Susceptibility

General Introduction

The socioeconomic effects from landslides are experienced around the world, due largely to the increased urbanization and development in landslide-prone areas. Construction of housing developments, industrial structures, transportation routes and facilities, mines and quarries, dams and reservoirs, and communications systems have disturbed large volumes of geologic material in an effort to meet the demands of population growth. Apart from contributing to the factors that cause slope failure, development in landslide-prone areas also increases the costs associated with these natural disasters. Often, landslide damage exceeds what is reported by news media because it is considered to be the result of a multi-hazard event, such as an earthquake (Schuster 1996). In particular, shallow slope instability remains a persistent obstacle in mountainous regions with shallow colluvial soils. Ultimately, reducing the devastating impacts from frequent landslide activity requires greater accuracy in predicting the size and location of a potential slide, providing motivation for research in landslide susceptibility mapping.

This thesis presents a manuscript that describes the development of a new shallow landslide model and its implementation as a framework for assessing shallow landslide susceptibility. The three-dimensional limit equilibrium model uniquely characterizes the influence of tree roots, seismicity, and topography as boundary forces. In addition, this model is applied within a Geographic Information System platform to represent shallow landslide susceptibility across a landscape scale.

Evaluation of Topography and Seismicity on Shallow Landslide Susceptibility: A Simplified Three-Dimensional Slope Stability Framework

Daniel M. Hess[1], Ben Leshchinsky[1], Michael Bunn[1], Michael J. Olsen[1], H. Benjamin Mason[1]

[1]Department of Civil and Construction Engineering, Oregon State University, Kearney Hall, Corvallis, Oregon, United States of America

Abstract

Shallow landslides are a prevalent concern in mountainous regions that can result in severe societal, economic, and environmental impacts. The challenge is further compounded as the size and location of a potential slide is often unknown. This study presents a generalized approach for evaluation of shallow landslide susceptibility using an existing shallow landslide inventory, remote sensing data, and various geotechnical scenarios. The three-dimensional limit equilibrium model uses a grid-based approach that uniquely incorporates tree root-reinforcement, earth pressure boundary forces, and pseudo-static seismic accelerations. Findings from this study include the back-calculation of soil strength from a landslide inventory, a convergence upon critical landslide size, and the determination of shallow landslide susceptibility for a landscape or infrastructure considering various root, water, and seismic conditions.

Introduction

Landslides are natural hazards that have major societal, economic, and environmental impacts on an international scale. In particular, shallow landsliding presents a persistent hazard, especially in mountainous, marginally stable regions with weak, yet critical root reinforcement. In seismically active areas, strong ground motions are also capable of destabilizing a slope that would normally be stable under static conditions. The size and location of a potential landslide can be unknown, which presents a significant challenge to engineers and can result in losses to infrastructure and human life.

Landslide susceptibility mapping is a method of identifying regions of slope instability based on probabilities of landslide occurrence. “Hazard map” is often used as a synonym for “susceptibility map,” however, the two should be distinguished. In particular, hazard maps are developed by considering the temporal occurrence or recurrence and magnitude of failure, and susceptibility maps consider only the magnitude of failure (Hervás and Bobrowsky 2009). Aside from qualitative susceptibility mapping (i.e., maps developed by allowing experience and judgement to dictate the spatial limits of a hazard), two main methods for creating quantitative susceptibility maps exist in practice: (1) the statistical method (Ayalew and Yamagishi 2005; Carrara et al. 1991; Dai and Lee 2002; Ohlmacher and Davis 2003; Xu et al. 2013), and (2) the deterministic method (Bellugi et al. 2015; Dietrich et al. 1995; Milledge et al. 2014; Miller and Sias 1998; Westen and Terlien 1996; Xie et al. 2006). The statistical method for creating susceptibility maps can include bivariate and multivariate approaches, which utilize the historical links between landslide distribution and the factors controlling a landslide. The deterministic method for creating susceptibility maps utilizes engineering properties of the soil (e.g., density, friction angle) to express instability as a factor of safety, which is defined as the ratio of forces resisting failure to forces driving failure (Ayalew and Yamagishi 2005).

An integral part of effective landslide susceptibility mapping is the use of Geographic Information Systems (GIS). In the past, GIS have primarily been used for displaying data and results, and not for manipulating data and extracting new information (Carrara et al. 1999). However, modern remote sensing techniques, such as Light Detection and Ranging (LIDAR), have made collecting elevation data for widespread areas easier. As a result, producing a raster grid of ground surface elevations, which is known as a Digital Elevation Model (DEM), has also become easier. Derivative products like slope and slope direction (i.e., aspect) can be calculated for each cell of a DEM. Accordingly, DEMs enable engineers to extract relevant slope-specific information which can be used to improve landslide susceptibility maps. Notably, each slope value is calculated by finding the maximum rate of change in elevation among neighboring cells in the DEM (Mahalingam and Olsen 2015); therefore, determining slope using GIS is highly dependent on the resolution of the parent DEM. Different DEM resolutions will produce

different values for slope, which will ultimately yield differing estimates of landslide susceptibility.

The deterministic method for assessing shallow landsliding is usually performed using two-dimensional (2D) limit equilibrium analyses, such as the infinite slope method, which can employ the raster structure of DEMs (Dietrich et al. 1995; Iida 2004; Tsai and Yang 2006; Westen and Terlien 1996; Wu and Sidle 1995). A fundamental assumption of the infinite slope method is that an infinitely-long planar slope surface fails along a single failure plane. Thus, lateral boundary forces are neglected during the analysis, which makes this a suitable analysis method for shallow landsliding on slopes characterized by consistent soil depths over broad regions. Although the infinite slope method is a relatively simple analysis method, comparison of results for infinite slope and finite element methods show that the infinite slope method is always suitable for the analysis of shallow landsliding on slopes with length to height ratios of 25 or larger (Milledge et al. 2012). In contrast, three-dimensional (3D) slope stability methods account for edge effects and yield higher factors of safety than 2D methods (Duncan 1996). An example of an edge effect considered in 3D methods is the lateral shear resistance generated by lateral earth pressure acting against the slope failure's boundary (Arellano and Stark 2000). Three-dimensional stability methods for shallow soils resemble a sliding block analysis, and have more recently been used to calculate factors of safety for a given DEM (Bellugi et al. 2015; Dietrich et al. 2007; Milledge et al. 2014).

When considering the stability of a slope, vegetation can motivate slope stability via mechanical reinforcement from the roots as well as modification of slope hydrology via moisture extraction. Researchers have investigated the mechanical stabilization of roots by way of modeling root-fiber soil interaction, conducting laboratory tests, and performing in-situ tests of root-permeated soils (Gray and Sotir 1996). The limit equilibrium theory developed by Waldron (1977) and Wu et al. (1979) focuses on the tensile strength of root fibers that penetrate the shear zone where sliding occurs, and the associated ratio of root area to soil area that occurs at this interface. Furthermore, by accounting for the angle of shear distortion, the tensile strength is resolved into shear strength components through a Mohr-Coulomb failure relationship. Initially, this concept was incorporated into the infinite slope method by increasing the shear resistance along the

planar surface at the base of a soil block. However, researchers have shown that the depth of root penetration remains shallow (< 2m) and the reinforcement from lateral roots plays a greater role in stabilizing landslides (Roering et al. 2003; Sakals and Sidle 2004; Schmidt et al. 2001; Schwarz et al. 2010). Despite the many studies that have measured the influence of roots on soil stability, spatial variability over a landscape remains a challenge for DEM-based landslide susceptibility mapping (Schmidt et al. 2001).

In contrast to the resisting strength of root cohesion, seismic influences have been applied to slope stability analyses as a driving component of failure. Pseudo-static analysis has been a common method for examining seismic slope stability and consists of applying inertial body forces—horizontal and/or vertical—to the failure mass of soil. Since this method only considers a single seismic coefficient for the analysis, the main limitation of this method is the ability of a single coefficient to represent the complex nature of an earthquake (Kramer 1996).

The present study attempts to approach shallow landslide susceptibility mapping in a new and comprehensive manner that is based on a 3D limit-equilibrium model applied within a GIS framework. The analysis incorporates boundary forces developed from surrounding topography, pseudo-static coefficients that change in magnitude and direction during an earthquake motion, soil depth and friction angle calculated from a GIS database of local shallow landslides, and a convergence on critical landslide size by analyzing DEMs of varying resolution.

Methodology

Derivation of the Three-Dimensional Topographic Limit Equilibrium Model (3DTLE)

The model developed herein for determining shallow landsliding potential, referred to as the Three-Dimensional Topographic Limit Equilibrium model (3DTLE), can be represented by the free-body diagram shown in figure (1). The 3DTLE model formulation employs many common assumptions associated with the infinite slope method; for instance, the failure body is a rigid block of homogenous soil, the landslide occurs along a planar slip surface, and seepage is

oriented in the slope-parallel direction. In contrast to the infinite slope method, the present model accounts for landslide width and multiple boundary forces.

Geometric properties of the soil block shown in figure (1) include the width, *X*; the slope-parallel length, *L*; the height, *H*; the slope angle, β (in degrees); and the water height ratio, *m*. Body forces include the soil weight, W_s, and the horizontal and vertical pseudo-static seismic forces, F_h and F_v. Boundary forces include the weight of trees, W_t; the normal force, *N*; the basal and side shearing forces, $S_b$and S_s; the root tensile force, T_u; and the lateral earth pressure forces, P_{side}, P_{up}, and P_{down}—acting with an inclination angle of δ (in degrees) on the side, upslope, and downslope surfaces, respectively.

Summing forces parallel to the basal slip surface results in,

$$S_b + 2S_s + T_u + \left(P_{down} - P_{up}\right)\cos(\delta - \beta) + (F_v - W_s - W_t)sin\beta - F_h cos\beta = 0 \quad (1)$$

and summing forces perpendicular to the basal plane yields,

$$N + F_h sin\beta + (F_v - W_s - W_t)cos\beta + \left(P_{down} - P_{up}\right)\sin(\delta - \beta) = 0 \quad (2)$$

For maintaining static equilibrium, it is assumed that the lateral earth pressure forces on the side surfaces, P_{side}, are equal in magnitude and opposite in direction; therefore, there is no movement in the x-direction. The resultant shear and tensile forces in equation (1) are expressed as stresses multiplied by the respective area over which they are applied; i.e.,

$$S_b = \tau_b XL \quad (3)$$

$$S_s = \tau_s HLcos\beta \quad (4)$$

$$T_u = \sigma_u HX \quad (5)$$

where τ_b and τ_s are the shear stresses on the base and side, respectively, and σ_u is the tensile stress on the upslope surface.

The shear stress on the failure plane is expressed as a shear strength divided by a factor of safety, which is common practice for most limit equilibrium analyses. The shear strength, S, of soil has

commonly been applied to effective stress slope stability analyses using the Mohr-Coulomb failure criteria,

$$S = c' + \sigma' tan\phi' \tag{6}$$

where c' is the effective soil cohesion intercept and ϕ' is the effective soil friction angle.

In contrast to a traditional Mohr-Coulomb failure criteria, the present model considers the strength of a combined soil-root system following the theory proposed by Wu et al. (1979). The theory states that the tension in a root fiber can be resolved into components parallel and perpendicular to the shear zone, and that a root's contribution to shear strength is given by,

$$S_r = t_r(cos\theta tan\phi' + sin\theta) \tag{7}$$

where t_r is the average root tensile strength per soil unit area and θ is the angle of shear distortion. S_r in equation (7) can also be referred to as root cohesion, c_r, which is often used in the analysis of shallow slope stability (Bischetti et al. 2005; Gray and Sotir 1996; Wu et al. 1979). Combining equations (6) and (7) with the safety factor produces the following expressions for the shear stress used in equations (3) and (4),

$$\tau_b = \frac{(c' + t_{rb}sin\theta) + (\sigma'_b + t_{rb}cos\theta)tan\phi'}{F_s} \tag{8}$$

$$\tau_s = \frac{(c' + t_{rs}sin\theta) + (\sigma'_s + t_{rs}cos\theta)tan\phi'}{F_s} \tag{9}$$

where t_{rb} and t_{rs} are the root strength terms corresponding to the base and side [obtained by solving for t_r in equation (7)], and σ'_b and σ'_s represent the effective normal stresses on the basal and side surfaces, respectively. Because the upslope surface is not a shearing surface, the root fibers do not experience lateral movement, and the roots' reinforcing strength is tensile. The tensile strength of the roots is defined by,

$$\sigma_u = \frac{t_{rs}}{F_s} \tag{10}$$

The normal stresses, σ'_b and σ'_s, in equations (8) and (9) are given by the following expressions,

$$\sigma'_b = \frac{N}{XL} - u_b \tag{11}$$

$$\sigma'_s = \frac{P_{side}}{HLcos\beta} \tag{12}$$

where the normal force, *N*, is obtained by re-arranging equation (2) as,

$$N = (W_s + W_t - F_v)cos\beta + \left(P_{up} - P_{down}\right)\sin(\delta - \beta) - F_h sin\beta \tag{13}$$

and the pore water pressure at the base, u_b, for seepage parallel with the slope is,

$$u_b = \gamma_w m H cos^2\beta \tag{14}$$

where γ_w is the unit weight of water.

Next, the body forces, F_h, F_v, and W_s, are defined as,

$$F_h = k_h W_s \tag{15}$$

$$F_v = k_v W_s \tag{16}$$

$$W_s = HXLcos\beta[(1-m)\gamma_s + m\gamma_{sat}] \tag{17}$$

where k_h and k_v are the pseudo-static seismic coefficients in the horizontal and vertical directions, respectively, and γ_s and γ_{sat} are the soil unit weights for dry and saturated conditions, respectively. The 3DTLE model ignores the effects of partially saturated soil (e.g. matric suction) and assumes that the soil below the phreatic surface is saturated and that the soil above is dry.

Finally, by substituting equations (3-5) and (8-17) into equation (1) and re-arranging, the following closed-form solution is obtained for the factor of safety against landsliding,

$$F_s = \frac{A_1 c' + A_2 XL t_{rb} + (2A_2 HLcos\beta + HX)t_{rs} + (A_3 + A_4)tan\phi'}{A_5} \tag{18}$$

where A_1 through A_5 are defined as,

$$A_1 = XL + 2HLcos\beta \tag{19}$$

$$A_2 = cos\theta tan\phi' + sin\theta \tag{20}$$

$$A_3 = HXLcos\beta[(1-m)\gamma_s + m\gamma_{sat}][(1-k_v)cos\beta - k_h sin\beta] + W_t cos\beta - \gamma_w mHXLcos^2\beta \tag{21}$$

$$A_4 = 2P_{side} + (P_{up} - P_{down})\sin(\delta - \beta) \tag{22}$$

$$A_5 = HXLcos\beta[(1-m)\gamma_s + m\gamma_{sat}][(1-k_v)sin\beta + k_h cos\beta] + W_t sin\beta + (P_{up} - P_{down})\cos(\delta - \beta) \tag{23}$$

Additionally, the weight of trees can be approximated by the following equation:

$$W_t = \frac{\pi}{4} {D_t}^2 H_t \rho_t N_t XLcos\beta \tag{24}$$

in which D_t, H_t, ρ_t, and N_t are average values for diameter, height, wood density, and number of trees per unit area, respectively. The estimation of tree weight in equation (24) is similar to the estimation proposed in Wu et al. (1979), except that Wu et al. (1979) considered a weight per unit area of root mat instead of a weight per unit area of slope. Regardless, comparable results are described in the results section of this study.

Lateral Earth Pressure

In order to characterize the lateral boundary forces, it is assumed that the earth pressure force acting on the upslope surface results from an active failure wedge, that the earth pressure force acting on the downslope surface results from a passive failure wedge, and that the earth pressure force at the side surfaces can be approximated by at-rest conditions. It should be noted, however, that significant movement is necessary to mobilize passive earth pressures, which implies that assuming at-rest conditions for the downslope margin is reasonable. Earth pressure theory is applied to the vertical surfaces of the soil block following Arellano and Stark (2000) and Milledge et al. (2014).

Although, the earth pressure theory used in 3DTLE remains unique in that it can employ active and passive seismic earth pressures and earth pressures that include the influence of adjacent topography. The at-rest earth pressure force acting on the side surfaces, P_{side}, is given by,

$$P_{side} = Lcos\beta \left[K_0 \left(\frac{1}{2}\gamma_s H^2 + qH \right) - \frac{1}{2} m^2 H^2 \gamma_w cos^2\beta \right] \quad (25)$$

where $K_0 = 1 - sin\phi'$ is the at-rest coefficient developed by Jaky (1944) for granular soil, and q is the spatially averaged soil surcharge at the lateral boundary due to adjacent topography. The surcharge imposed at the lateral boundary is calculated through bilinear interpolation of the given digital elevation model. More specifically, a subroutine obtains elevations for the midpoint of the lateral boundaries considering the rotation of each pixel to coincide with the slope direction (i.e., aspect). The difference between the elevation of each pixel and the elevation of a point along the lateral edge is multiplied by the soil unit weight to obtain a soil surcharge. As mentioned previously, lateral forces at the sides must be equal in magnitude, so an average is taken of the two elevation differences. Equation (25) was developed for horizontal soil; accordingly, soil surcharge can result from concave topography [i.e., when lateral elevations are above a cell's elevation, producing a positive surcharge (Figure 2)] or convex topography (i.e., when lateral elevations are below a cell's elevation, producing a negative surcharge). The first and second terms inside the brackets of equation (25) represent the force per unit length due to soil and water, respectively, and the term outside the brackets is the length over which the lateral earth pressure force acts.

Shukla (2015) and Shukla (2013) provide a framework for computing pseudo-static active and passive earth pressures for *c'- ϕ'* soils assuming a planar failure surface. The equations presented by Shukla also include a soil back-slope above the failure wedge. The soil back-slope is approximated by the slope of the considered pixel—a positive back-slope for the active wedge and a negative back-slope for the passive wedge. Since the slope of each pixel is calculated based on the surrounding elevations, adjacent topography serves to increase active pressure and decrease passive pressure at the upslope and downslope surfaces, respectively. Importantly, the Shukla seismic earth pressure equations were developed for dry soil. Simple modifications can be made to better represent a soil block with a phreatic surface. Kramer (1996), for instance, proposes using an average value for soil unit weight and adding a hydrostatic thrust term to the computed soil thrust. It should also be noted that the Shukla framework for determining pseudo-static active and passive earth pressure, and thus the 3DTLE model, does not consider the

dynamic response of pore water or the degradation of soil strength that can take place during strong ground motions.

Usually, the assumption of a planar failure surface results in overestimation of the passive pressure when the angle of interface friction, δ, is large. For instance, when δ is greater than approximately one-third of the soil's effective friction angle, the passive pressure for a planar failure surface can be significantly overestimated (Choudhury et al. 2004). An improved estimate of passive earth pressure can be obtained with a theory that incorporates a curved or composite failure surface; e.g., a log spiral surface (Milledge et al. 2014). Although the assumption of a planar passive wedge can overestimate earth pressures for certain cases, the planar passive wedge assumption yields a closed-form calculation of the factor of safety, which is necessary to facilitate reasonable computing times for analyses utilizing large DEMs.

Application of 3DTLE Model

Geospatial Data

Shallow landsliding is prevalent in the Oregon Coast Range of the United States, demonstrated by spatial data of landslide deposits through the Statewide Landslide Information Database for Oregon (SLIDO). The SLIDO database contains polygons of past landslide deposits that have been located from published maps as well as various attributes such as landslide movement type and depth of failure (Burns et al. 2008). In addition, the Oregon Department of Geology and Mineral Industries (DOGAMI) provides bare earth DEMs, which exclude vegetation. The 0.9 m (3 ft) resolution DEMs are produced from LIDAR point clouds and are available for much of Western Oregon.

To demonstrate the 3DTLE model, a location near Gales Creek, Oregon was selected, because of the availability of LIDAR data and because the density of the landslide inventory was robust. Located approximately 50 km (30 mi) west of Portland, the selected area features a narrow valley flanked by steeper forested slopes. State Highway 8 and Gales Creek run the length of the valley, and several smaller roads connect the scattered properties that lie within the valley and upon the hillslopes. Figure (3) shows the extent of the considered DEM as well as the considered shallow landslide deposit polygons. In addition to the selected rectangular tile near Gales Creek,

analyses were extended to assess landslide susceptibility for the larger, adjacent Gales Creek watershed that contains portions of Highway 6 and Highway 8. Six 7.5 minute quadrangle DEM tiles were used to perform a susceptibility analysis and then combined to form a composite map, demonstrating the applicability of the 3DTLE model to a regional scale. Additionally, road networks within the Gales Creek watershed were considered in an analysis of infrastructure risk.

Soil and Root Properties

A critical component of evaluating slope stability is the use of appropriate soil shear strength parameters. The 3DTLE model was applied to the landslide inventory to characterize soil strength for the regions of interest. To facilitate back-calculation of representative soil strengths, the following assumptions were made: (1) landslide deposit attributes like failure depth, slope, and area approximate pre-failure conditions; (2) the polygon area representing shallow landslide deposits has a square shape for a given body of rupture; (3) selected landslide records failed under static conditions, i.e. k_h and k_v are equal to zero; and (4) the soil is unconsolidated and mobilized drained soil strength conditions at failure (i.e., only ϕ' was used). With the aforementioned assumptions, the soil strength was back-calculated by assuming a factor of safety of unity for a set of landslide dimensions. Soil unit weights for dry and saturated conditions are assumed to be 15 and 16 kN/m^3, respectively, based on values published in Wu and Sidle (1995) for a study site near Mapleton, Oregon. The assumptions, of course, are an idealized representation of regional soil conditions, but present a means of using the regional slope stability model to attain meaningful data for susceptibility mapping; that is, a user may select appropriate soil conditions based on site investigations or back-calculated failures. Notably, for the current study, geologic and lithologic conditions were not directly modeled. In addition, the soil surcharge term was neglected during calculation of the lateral earth pressures because a pre-slide DEM was not available.

Back-calculation of soil strength using the landslide inventory requires an understanding of tree properties, and most notably, the root cohesion. Values of root cohesion can vary depending on tree species, age, environment, and considered scale. Sakals and Sidle (2004) applied a spatially variable model to determine root cohesion in the Oregon Coast Range and calculated 4.4 kPa for

natural forest. Roering et al. (2003) back-calculated a root cohesion of 11 kPa when applying a spatially variable model to a measured landslide in the Oregon Coast Range. The current study uses a root cohesion value of 8 kPa, which is approximately the mean of the values reported by Sakals and Sidle (2004) and Roering et al. (2003). Best estimates of tree properties for the Oregon Coast Range are defined as: D_t = 0.75 m, ρ_t = 6 kN/m^3, H_t = 40 m, N_t = 400 stems/ha, d_r = 1 m, and θ = 60^o, as described in previous studies (Roering et al. 2003; Sakals and Sidle 2004; Wu et al. 1979). Note that the depth of root penetration is one meter; therefore, root cohesion is only calculated over a one meter depth, and then applied as an equivalent strength to the full height of the soil block. Using the listed properties, the weight of trees per unit area is calculated as 4.4 kPa, which is similar to the 5.2 kPa value reported by Wu et al. (1979). Tree weight values, presented in equation (24), were assumed to correspond to the average root cohesion of 8 kPa, and scale by a factor of $c_r/8$; this enables adjustment in a parametric analysis, albeit linear for varying forest density or age.

A challenge related to back-calculating soil strength for large landslide inventories is the lack of knowledge concerning the landslide conditions at failure, and the need to use "aggregated" parameters to represent large regions. Accordingly, the sensitivity of back-calculated soil strength was determined for 100 representative shallow landslides by varying input parameters—including water height ratio and root cohesion. The sensitivity analysis produced a suite of mean friction angle values, which are shown in figure (4) as a function of water height ratio and root cohesion. For demonstrative purposes, the baseline conditions for the shallow landslide inventory were considered to be 8 kPa of root cohesion (forested conditions at failure) and a water height ratio of 0.5 (a relatively high water table), corresponding to an effective friction angle of 32.5 degrees. Since the time and conditions of each unique slope failure is unknown, one may choose conditions observed in recent, well-documented landslides; however, selection of these values can have significant implications on soil strength and subsequent susceptibility mapping. This approach presents a means of selecting an array of soil strength properties based on past landslides that may be more representative of a region.

Analysis of Landslide Size and Shape

Prior to applying the developed model to the SLIDO database, the second assumption used in the back calculation of soil strength was investigated by bounding each landslide inventory polygon with a rectangle. The side lengths of the rectangles were determined in ArcGIS using the Minimum Bounding Geometry tool, which fits multiple rectangles to a given polygon and selects the one with the smallest area. Based on the prevailing aspect, these dimensions were characterized as being parallel or transverse to the direction of motion. Finally, the ratio of the two dimensions for every fitted rectangle was compared with a probability density function (PDF) and a cumulative distribution function (CDF).

Within the 3DTLE model, the failure area is limited to the size of each pixel in the given DEM. Critical landslide size is unknown prior to performing the analysis, so it is necessary to evaluate a range of failure sizes through the input of several DEM resolutions. CDFs were developed for a given suite of DEM resolutions to investigate the relationship between pixel size and failure probability. First, CDFs of the landslide inventory were made by invoking the previous assumption that the polygons can be modeled as squares, which enables direct analysis within a gridded raster. An approximate pixel dimension for each landslide in the inventory was then calculated as the square root of the polygon's area. The resulting CDF conveys the percentage of landslides that occurred for a given pixel size. Next, the 3DTLE model was used to calculate areas of failure for a suite of ten DEMs ranging from 3 to 140 meters (10 to 450 feet) in resolution. Based on preliminary calculations, analysis with the source resolution (1 meter) was deemed too computationally expensive and did not produce significant results, so a bilinear resampling technique produced the range of considered DEM resolutions. The 3DTLE model was applied using the baseline value for back-calculated soil strength and a mean depth of failure as the soil depth. The total failed area calculated for each map was divided by the total failed area for all ten maps to obtain the percentage of failure that each pixel size contributed, thus producing a CDF when these percentages are cumulatively summed. Finally, input parameters like root cohesion, water height ratio, and horizontal seismic coefficient are varied to show their effect on calculated failure area.

Susceptibility Analysis

In this analysis, landslide susceptibility was founded on the shallow landslide inventory obtained from SLIDO. Back-calculated soil friction angle and depth of failure were treated as variables having certain probability distributions. The respective combination of a given friction angle and potential depth of failure (both corresponding to a specific probability) were used as input for a given slope stability analysis. Due to the inherent reliance on back-calculated strength and landslide depth for input, this susceptibility analysis is heavily dependent on the reliability of the landslide inventory.

To apply susceptibility mapping, distributions of landslide depth and back-calculated friction angle were divided into ten bins, with each bin having a mean value and an associated probability of occurrence. The model was run 100 times for each combination of friction angle and depth for four different DEM resolutions. The selected resolutions—6, 18, 30, and 61 meters (20, 60, 100, and 200 feet)—were considered representative of the baseline CDF curve, as highlighted in the results section. Varying pixel sizes were integrated into a singular susceptibility map by overlaying the calculated areas of failure with a resolution equal to the smallest cell dimension. If failure ($F_s < 1$) was calculated for a given cell, then the cell was assigned the product of the two probabilities, friction angle and depth, that were used in its calculation. Finally, the probabilities were summed for a given cell, producing a map where each cell has a probability of failure between 0 and 100%.

In addition to the rectangular DEM, the same susceptibility analysis was also applied to tiles of the Gales Creek watershed to exercise applicability on a larger scale. The watershed was delineated using the ArcGIS Hydrology toolset with a 6 m (20 ft) resolution DEM. The selected DEM encapsulated all portions of the Gales Creek drainage located North of Forest Grove, Oregon. The tile discretization produced six irregularly shaped tiles, which caused erroneous susceptibility calculations at the tile margins; i.e., slope cannot be accurately computed at the edges and impairs the factor of safety calculation. Thus, a buffer of 150 meters (492 feet) was removed from the map to eliminate false representations of the failure probability.

Finally, risk was characterized for named roads within the watershed as a means of evaluating the impacts of shallow landsliding on regional infrastructure lifelines. Included roads are those owned by Metro regional government, the Oregon Department of Transportation, the Oregon

Department of Forestry, Washington County, and the City of Forest Grove (Oregon Geographic Information Services Unit, 2014). The risk was represented as the maximum probability of failure occurring within 15 meters (50 feet) of the roadway's centerline under the conditions of each susceptibility map. The infrastructure risk mapping that was performed accounts for failures that develop under the roadways or in close proximity, but it does not account for slope failures further than 15 meters away that have significant runout distances.

Seismic Analysis

The detrimental effects of an earthquake on slope stability can be analyzed by using dimensionless pseudo-static seismic coefficients, k_h and k_v (for the horizontal and vertical directions of shaking, respectively). These coefficients can be estimated from the amplitude of a target acceleration time-series. In practice, k_h and k_v are applied equally to all potential slope failures due to the inherent complexity of earthquake ground motions and the uncertainty with determining realistic motions for a given site. However, peak ground accelerations are intrinsically direction-dependent, i.e., higher accelerations develop in certain directions over the time of a given earthquake motion. Hence, a more realistic seismic slope stability analysis would consider both the direction-dependent and time-dependent changes of the pseudo-static seismic coefficients for the duration of an earthquake motion. Herein, susceptibility analyses for direction- and time-independent pseudo-static seismic coefficients (i.e., the common uniform assumption) as well as susceptibility analyses for direction- and time-dependent coefficients were undertaken to evaluate the effects of assuming a uniform pseudo-static seismic coefficient. Obtaining a representative strong motion record for the susceptibility analysis required filtering a database of past earthquake motion records. The filtering criteria were developed so that selected earthquake motions shared important characteristics as the expected earthquake motion at the study site; primarily, similar tectonic regime, moment magnitude (M_w), and site to source distance. The Cascadia Subduction Zone lies in close proximity to the study area, meaning that potential fault activity is capable of producing earthquakes with larger magnitudes and greater durations than shallow crustal earthquakes, due to the greater capacity for building up strain energy (Kramer 1996).

In common practice, a suite of representative earthquake motions is chosen for seismic slope stability analyses; however, one earthquake motion is selected herein to highlight the analysis framework. A design response spectrum for the study site, which was developed using the American Society of Civil Engineers (ASCE) 7-10 guidelines (ASCE 2013) and the United States Geologic Survey (USGS) seismic design maps, was used to attain the chosen earthquake motion. To develop the target design spectrum, a soil site class D was assumed (ASCE 2013). Next, a suite of 46 subduction zone earthquake motions recorded during the 2011 M_w9.0 Great East Japan Earthquake, which is the same suite used by Carey (2014), were chosen to use in a scaling algorithm that matched the median response to the target design spectrum. The earthquake records were obtained from both KiK-net and K-NET recording networks, and were filtered with fourth order Butterworth filters in the time domain using motion-specific corner frequencies (Carey 2014). Furthermore, the motions were digitized with a sampling frequency of 100 Hz.

From the 46 earthquake motion records, one East-West (EW) and one North-South (NS) motion were chosen. In general, the response spectrum of an earthquake motion was compared to the developed site-specific target spectrum, and the earthquake motions were linearly-scaled in the time domain to improve their match to the target spectrum. The earthquake motion selection algorithm was similar to algorithms presented by Barbosa et al. (2014) and Kottke and Rathje (2008): i.e., minimize the root-mean-squared-error (RMSE) between the selected earthquake motion response spectrum and the target spectrum over a chosen period range, and show preference to linear scaling factors closer to unity. Depicted in figure (5) with scaled amplitudes, the two motions represent potential seismicity near Gales Creek, OR. The low scale factors (1.8 and 2.0 for EW and NS, respectively) translate to scaled motions that closely approximate the physical accelerations that were recorded; as opposed to creating a more unrealistic motion with larger scaling factors. The two motions were also selected based on low values of RMSE, meaning that the scaled motions were closer to matching the target response spectrum. The acceleration-time histories were further described by the ground motion intensity measures listed in table (1), where it can be seen that PGA values for both components are below 0.25 g with significant durations of approximately 70 seconds.

From the selected earthquake motion acceleration-time series, each acceleration value (in *g*) corresponds to a dimensionless k_h that was applied to the 3DTLE model to evaluate the effects of acceleration direction and slope aspect on landslide occurrence. At a given time increment, the 3DTLE model used a horizontal pseudo-static seismic coefficient for a given cell. The cell-specific horizontal seismic coefficient was implemented using a subroutine that projected a given EW and NS pair of k_h values to coincide with a pixel's aspect, i.e., adding the two projected values to obtain a single seismic coefficient for a single pixel. In this manner, each cell of a DEM has a unique horizontal pseudo-static seismic coefficient that was used for the factor of safety calculation. For the seismic analysis, mean depth and mean back-calculated strength were used as opposed to the probability distributions used for the susceptibility analysis.

Similar to the susceptibility analysis, four DEM resolutions were used to calculate regions of failure and overlaid onto one map. This process was repeated for each time step of the earthquake motion to produce an animation of cumulative failed area. An analysis of the full 300 second motion produces 30,000 frames, resulting in considerable computing expense. Accordingly, a reduced motion and a smaller DEM tile were used for the seismic analysis—the smaller DEM tile can be seen in the upper left quadrant of the larger tile shown in figure (3).

Overview of Analyses

The flow chart depicted in figure (6) provides a simplified illustration of the various steps that make up the presented framework. Three main input sources—shallow landslide inventory, DEMs, and earthquake records—enable the three primary forms of analysis in this idealized representation. Calculation with the 3DTLE model was performed with MATLAB R2015b software while ArcGIS 10.2.2 software allowed for manipulation of spatial data and generation of select map figures. Additionally, SeismoSignal 2016 software assisted with characterization of ground motion intensity measures for the two acceleration time histories. All of the analysis took place on a computer with 128 GB of RAM and two processors running at 2.6 GHz, using the Windows 7 operating system. Computation time varied for each step of the process (directly related to the size of input DEMs), and as a result, certain tasks were either subdivided into

shorter computations or calculated in parallel. As an illustration of computation time, performing the product distribution and generating susceptibility maps for 48 combinations of k_h, m, and c_r took approximately 52 hours.

Results and Discussion

Landslide Size and Shape

Results from the investigation of the square area assumption with landslide deposit polygons can be seen in figure (7). The map on the left is a depiction of fitting rectangles to the polygons, while the plot on the right represents the probability of occurrence for rectangles with different ratios of parallel to transverse dimension. The data was fit with a lognormal distribution after the exclusion of outlier data that constituted seven percent of the original sample size. This plot demonstrates a mean length to width (L/W) ratio of 1.53 and a peak probability for a ratio of approximately 1.0. However, it should be noted that implicit consideration of (1) an active, driving wedge at the top of the landslide body, (2) a passive, resisting wedge at the toe, and (3) actual length of a given landslide body being greater than its square projection due to slope demonstrate L/W ratios greater than unity, similar to observations made in prior literature (e.g. Milledge et al. 2014, where L/W for several inventories was primarily between one and two). These observations deemed the 3DTLE approach suitable for evaluating shallow landslide susceptibility using a grid-based framework.

To observe sensitivity of input parameters on landslide size, a range of input root cohesions, water height ratios, and horizontal seismic coefficients were also applied to demonstrate the effect on calculated failure area, highlighting larger effective landslide areas for higher water heights and seismic coefficients. This dependence of failure on pixel size is illustrated by the CDF's in figure (8). The baseline scenario and inventory are represented in all three plots while considered input values range from 0 to 50 kPa for root cohesion, 0 to 1 for water height ratio, and 0 to 0.3 for horizontal seismic coefficient. The curvature of the CDFs depicted in each of the three plots provides a relative measure of which pixel sizes are causing the most failure; steeper curves translate to a majority of failures caused by a small range of cell sizes, while a curve with

a more shallow gradient signifies that many cell sizes contributed to the calculated area of failure.

Root cohesion had minimal effect on the distribution of failure among pixel sizes as evidenced by the similar trend of the closely spaced CDFs (Figure 8a). While the increase of root strength decreased observed failures, it did so evenly amid the ten considered DEM resolutions. Figure (8b) shows the variation of the water height ratio, which greatly affect the size of predicted failure. For m = 0, approximately 90% of the failures took place for pixel sizes less than 30 meters (100 feet) with a mean pixel dimension of 10 meters (32 feet), while full saturation (m = 1) demonstrated failure that was distributed across significantly larger pixel sizes (mean of 35 meters). The addition of seismicity (Figure 8c) revealed an increase in landslide size; increasing k_h from 0 to 0.3 increased failure among larger pixel sizes, representative of a mean landslide dimension changing from 25 to 32 meters (82 to 105 feet). For the baseline case, approximately 90% of the failures occur from pixel dimensions less than or equal to 60 meters (200 feet).

Susceptibility Analysis

Based on the results of the analysis of landslide area, four different DEM resolutions were determined to be the most critical and selected for generating susceptibility maps: 6, 18, 30, and 60 meters (20, 60, 100, and 200 feet). Along with these DEMs, depth and friction angle distributions from the shallow landslide inventory were used to calculate a product distribution. The distributions of back calculated friction angles and depths were divided into ten bins with mean values ranging from 10.5 to 55.5 degrees for the friction angle (Figure 9a) and 1.1 to 4.4 meters (3.6 to 14.4 feet) for depth (Figure 9b). The selected distribution of effective friction angles was back-calculated for the baseline scenario.

Together, the four DEM resolutions and distributions of both landslide depth and friction angle were applied to produce susceptibility maps for different variations of horizontal seismic coefficient, water height ratio, and root cohesion. Considered input values included: $k_h = 0$, 0.1, 0.3, 0.6; m = 0, 0.25, 0.5, 0.75; and $c_r = 0$, 8, 20 kPa. Four examples of the produced susceptibility maps are shown in figure (9), where map colors range from dark blue (0% probability of failure) to dark red (100% probability of failure). Within figure (10), the two maps

on the right have an increased water height ratio and the two maps along the bottom have an increased seismic coefficient. The increased height of water and seismicity caused an increase in the probability of failure for the sloped terrain along the edges of the valley. To quantify the effect of changing input values, the mean probability of failure is compared for the 48 different combinations of k_h, m, and c_r (Figure 11). The mean probability of failure for the represented scenarios is directly proportional to the water height ratio and horizontal seismic coefficient, but inversely proportional to root cohesion. For $k_h = 0.6$ and m = 0.75, mean failure probabilities are greater than 90%—signifying that most of the map has a high probability of failure.

The results of susceptibility mapping at the watershed scale can be seen in figures (12) and (13), highlighting the notable impacts that seismicity may have in mountainous terrain with marginally stable slopes. Four cases of horizontal seismic coefficient, water height ratio, and root cohesion were considered in the calculation of failure probabilities, each showing increasing probability of failure with greater seismic accelerations. Omission of root cohesion demonstrated a small increase in landslide susceptibility, but did not have as large of an impact as seismicity. This increasing susceptibility of failure under earthquake accelerations translates directly to greater risk towards infrastructure (Figure 13). Roads that were influenced most were located on or adjacent to steep hillsides that were deemed likely to fail. As horizontal seismic coefficients increased, roads that were in proximity to gentler slopes realized greater risk from landslides. For simplicity in visualization, risk probabilities for the roadways were classified into 25% intervals from 0 to 100%.

Seismic Analysis

Effort was made to calculate the factor of safety at every time step of the earthquake motion to avoid aliasing the signal, ensuring that local and global peak accelerations were considered in the analysis. Due to this increased computation, the motions were clipped to 122 seconds so that their respective k_h values could be applied to the shallow landslide model, producing a map of cumulative failed area for every time step. The resulting motions begin with static conditions and end when the seismic influences are no longer affecting the calculation of failure. The flat sections of each curve shown near the end of the motion in figure (14) are a good indicator that

the significant effects of the earthquake have already been captured by the 3DTLE model; large accelerations correspond to jumps in the cumulative failed area. Final calculated areas of failure for maps produced by the four combinations of m and c_r, listed in figure (14), are approximately 222,740 m^2 (7.10% of map area), 196,840 m^2 (6.28%), 337,500 m^2 (10.8%), and 326,610 m^2 (10.4%), respectively. From this it can be surmised that increasing the water heights increases the magnitude of calculated failure, while root strength plays a role in preventing seismically-induced shallow landslides.

This process for assessing seismic landslide susceptibility—with horizontal seismic coefficients projected to correspond with aspect—was distinct from that of applying a single seismic coefficient. With a single coefficient to represent an earthquake (often the PGA is selected), the analysis applies the full acceleration value to every pixel in the direction of the slope, resulting in the most severe case when considering the forces driving failure. In contrast, the present seismic analysis incorporates a more realistic scenario for the determination of failure, based on the degree to which the direction of seismic acceleration aligns with the direction of the slope. Since every slope direction for a given DEM would likely not be represented in the brief moment that peak accelerations are realized, it is therefore over-conservative to apply a peak value to every pixel.

Comparison to Conventional Infinite Slope Analyses

As cited previously, conventional analyses of shallow landslide susceptibility have often been applied using the infinite slope method, prompting a comparison of 3DTLE for notable differences. The comparison looked at landslide susceptibility for four combinations of horizontal seismic coefficients and water height ratios, using the binned distributions of friction angle and landslide depth while employing the infinite slope equation developed by Hadj-Hamou and Kavazanjian (1985). This form of the infinite slope accounts for slope parallel seismic accelerations, so the magnitude of the input horizontal seismic acceleration was projected to a slope parallel direction to maintain consistency. Furthermore, the infinite slope analysis does not include any root reinforcement along the basal shearing plane as do other forms of the infinite slope (Dietrich et al. 1995), mainly because the considered depths greatly exceeded the realized

depth of root penetration ($d_r = 1m$). Vertical surcharge from tree weight is also neglected in the simplified infinite slope model.

A raster subtraction was employed to observe the spatial impact of the infinite slope model's assumptions versus those demonstrated by the inclusion of boundary forces (Figure 15). Subtracting the 3DTLE failure probability from the infinite slope calculated probability produced a map of probability differences; a positive difference signifies that the infinite slope model calculates a higher probability of failure, whereas a negative difference denotes higher probabilities calculated with the 3DTLE model. The 3DTLE model calculated probabilities of failure for $c_r = 0\ kPa$ to maintain correlation with the infinite slope model that neglects root cohesion.

As described at the beginning of this study, 2D analysis methods like the infinite slope will calculate lower factors of safety than 3D methods—meaning that the infinite slope analysis should predict higher probabilities of failure than 3DTLE. For static cases, infinite slope analyses predict higher susceptibility to landsliding, both with and without the presence of water (Figure 15). Although, analysis of m = 0.25 under static conditions does begin to demonstrate higher susceptibility from 3DTLE analysis, likely due to increased failures for relatively shallow cells that share a boundary with a steep cell at its toe (e.g. adjacent to "free faces"). This situation exhibits relatively larger driving forces from upslope water and lowered resistance from downslope passive resistance. As the factors driving failure are increased (water height ratio and seismic coefficient), the 3DTLE model produces more regions with higher failure probabilities. Similarly, this is likely due to the lack of downslope support, but also increased sensitivity to seismic accelerations which manifest not only as a body force in the potential landslide body, but as driving forces in both the neighboring active and passive wedges.

Considerations for Applying 3DTLE

Mean back-calculated friction angles [e.g. figure (4)] may span a large range of values depending on the input parameters and the given landslide inventory, making it difficult to find a singular value for evaluating regional landslide susceptibility. The water height ratio appears to have a major influence on this determination based on the change in back-calculated strength between

$m = 0$ and $m = 1$, yet varying root cohesion also affects the back-calculated strength—especially when m is large. Choosing m = 0.5 as the water height ratio for the baseline case was an example of selecting a representative soil strength and applying it to the multi-staged analysis. Although, a half-saturated soil depth can be a reasonable notion due to landslide triggering often occurring during periods of intense rainfall and soil saturation (Bellugi et al. 2015; Dai and Lee 2002; Iida 2004; Tsai and Yang 2006; Wu and Sidle 1995).

A reliable shallow landslide inventory is an integral part of assessing landslide susceptibility, and as such, the results rely heavily on its applicability to the analysis. The 3DTLE method assumes that inventoried landslide deposits can be modeled as having a square shape which affects the back-calculated soil strength, and it was determined that the mean ratio of landslide dimensions was roughly 1.5 (Figure 7). Because the polygons represent landslide deposits and not the pre-failure soil mass, it is most likely that the shape of the pre-failure soil mass was closer to that of a square, and failure caused an increase in the dimension parallel to movement. This statement is consistent with the idea that landslide movement can cause the soil to dilate, increasing the volume of soil being displaced (Cruden and Varnes 1996). While the shallow landslide deposit polygons vary in shape, the data presented in figure (7) and the implicit use of active and passive wedges at the upper and lower boundaries of a slide support the assumption of a square shape for the purpose of applying the grid-based 3DTLE model.

Moreover, a landslide inventory is a useful tool for performing this analysis, but it is not without error and uncertainty. Since the many landslide records are based on observations from published maps, it is quite possible that many smaller slope failures were not noticed or visible, meaning that the distribution of landslide area is shifted towards larger sizes. This would imply that the shallow landslide inventory CDF presented in figure (8) is also shifted to the right, corresponding to larger pixel sizes. This concern further supports the selection of $m = 0.5$ and $c_r = 8\ kPa$ as the representative scenario since this baseline CDF is positioned to the left of the inventory CDF in each plot. If the baseline CDF is thought to have aligned with the inventory CDF then it could be regarded as a more accurate representation of actual landslides in the Gales Creek area.

Using the soil strength and depth distributions of the shallow landslide inventory, corollaries were made about the statistical probability of slope failure occurring, resulting in susceptibility maps for various root, water, and seismic scenarios. The 48 different scenarios featured in figure (11) were investigated as a parametric study with input parameters that can change with environmental factors or be difficult to estimate on a landscape scale. However, scenarios with an input water height ratio of one were excluded from the susceptibility analysis because of the impractical nature of having the water table at the ground surface in mountainous terrain as well as for expediency in reducing computational expense. Furthermore, it is worth noting that root cohesion would have a larger effect on landslide susceptibility for shallower slides—when the landslide depth is less than the depth of root penetration and basal root reinforcement can be applied to the 3DTLE model. The generated susceptibility maps, such as those of figure (10), provide crucial information about shallow landslide susceptibility, namely, the spatial extent and magnitude of failure probabilities. Regions with high probabilities of failure can be identified over large extents, yet, the accuracy of a given map is dependent on the accuracy of a single parameter (friction angle, root cohesion, soil depth, water height ratio, etc.) to characterize the considered landscape.

Finally, the watershed maps of figures (12) and (13) include a significantly larger area than the rectangular maps of figure (10), which means that the watershed susceptibility relies on an inventory that is only partially representative of the landscape. Despite this notion, the main objective of this process is that shallow landslide susceptibility can be characterized for large extents based on given distributions. Accurate representation between the considered inventory deposits and the mapping extents should be maintained, which is usually accomplished by considering mapping extents with similar conditions as the inventory (lithology, soil type, hydrologic conditions, etc.). The main advantage of extending a mapped area is that meaningful conclusions can be made in areas where shallow landsliding may not yet have occurred. For instance, the road risk maps of figure (13) can aid in asset management decisions and emergency repair. While road risk maps display similar probabilities of failure as the watershed susceptibility maps, they capture the potential for infrastructure loss associated with nearby shallow landslides.

Conclusion

This study presents a framework for assessing shallow landslide susceptibility, based on the developed 3DTLE model, a shallow landslide inventory, LiDAR-derived DEMs, and various geotechnical scenarios. This shallow landslide model is unique in that it accounts for lateral root reinforcement along multiple surfaces, it characterizes the influence of adjacent topography through the earth pressure boundary forces, and that it may capture seismic influence in a manner more robust than typical pseudo-static analyses. Notable conclusions include:

- For certain landslide inventories, shallow landslide susceptibility may be sufficiently modeled using a grid-based structure to approximate landslide shape, particularly when accounting for implicit boundary wedges (active and passive) and basing the shape on post-rupture landslide remains, which are often marked as one shape despite possible runout and dilation during failure.
- The results of this multi-stage approach have shown that landslide susceptibility can be determined for the landscape scale with reasonable input parameters, particularly those from existing landslide inventories. This study presents an integrated approach to using existing landslide inventories to determine probability distributions of landslide depth, landslide size, and back-calculated soil shear strengths for a more meaningful approach to landslide susceptibility mapping under both static and seismic conditions. This analysis can be further translated into risk maps when considering proximity of landslide hazards to infrastructure or residential areas—a potentially useful asset management tool.
- Accounting for aspect- and time-dependence of seismic motions will provide significant differences in landsliding; however, extreme uncertainty in realized earthquake motions inhibit direct applicability in predicting failures.
- Use of a multi-dimensional slope stability tool can better capture the effects of topographic features including free faces, valleys, and ridges than conventional infinite slope methods, which are often conservative under seismic conditions as they cannot capture the effects of increased driving forces (upslope active wedge) and decreased resisting forces (downslope passive wedge) under inertial loading.

Examples of future work with shallow landslide susceptibility mapping involve refinement of the 3DTLE model. Root reinforcement can be analyzed in a way that captures the variation in root area ratio with depth as well as the progressive failure that develops from the stiffness of different sized root fibers. A more accurate characterization of passive pressure can be obtained by considering a curved failure surface. Finally, incorporation of unsaturated soil mechanics and hydrologic modelling may help capture the effects of partial saturation and infiltration, yielding better understanding of rainfall-induced landslides, a major driver in slope failures.

Figures

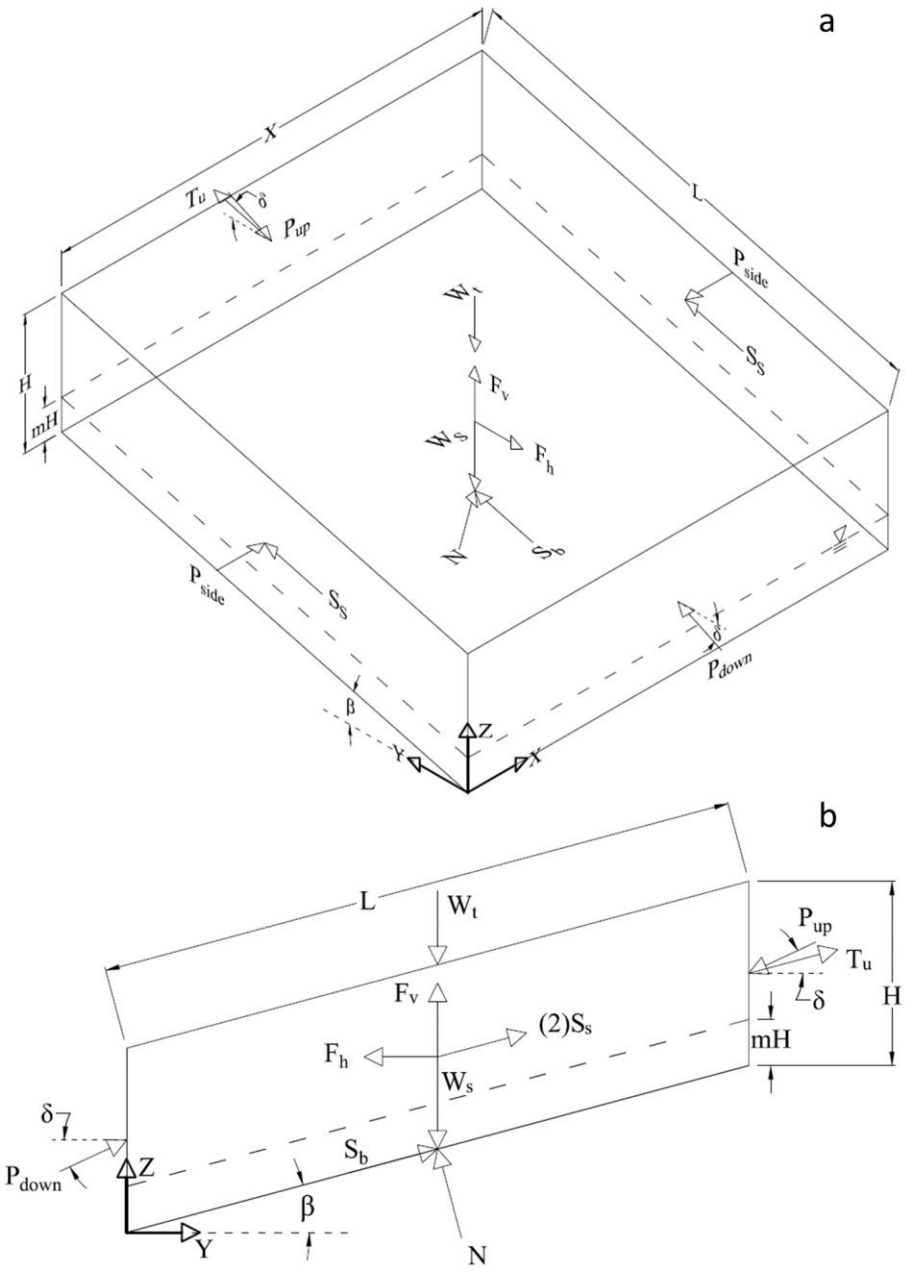

Figure 1. (a) Isometric and (b) profile views of the proposed soil block with associated dimensions and forces.

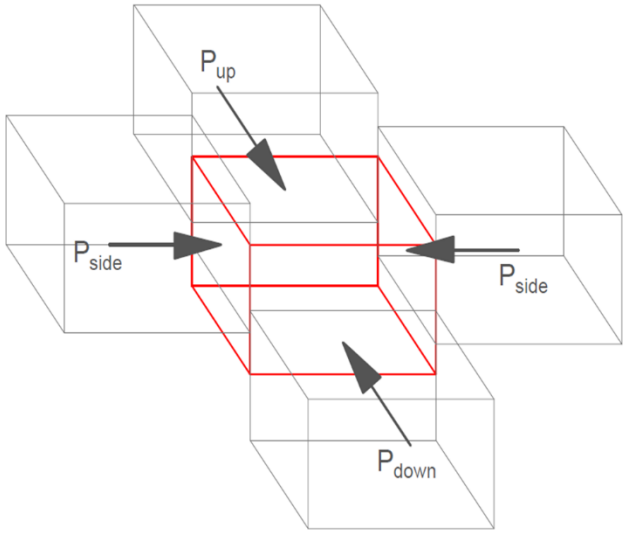

Figure 2. Example of concave topography with the two side pixels at higher elevations than the center pixel. The shown boundary forces are due to lateral earth pressure.

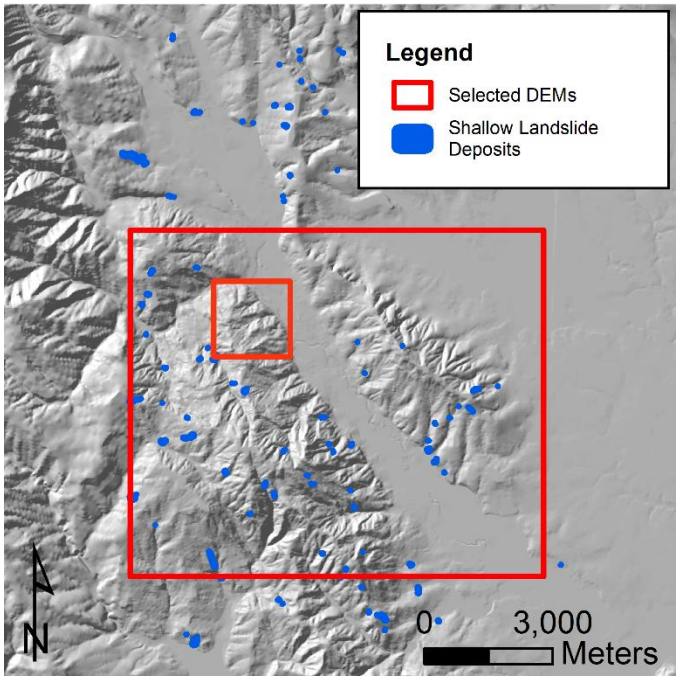

Figure 3. Shaded relief map of a portion of the Gales Creek quadrangle showing the limits of the selected DEMs and considered shallow landslide deposits. The smaller DEM is used in the seismic analysis.

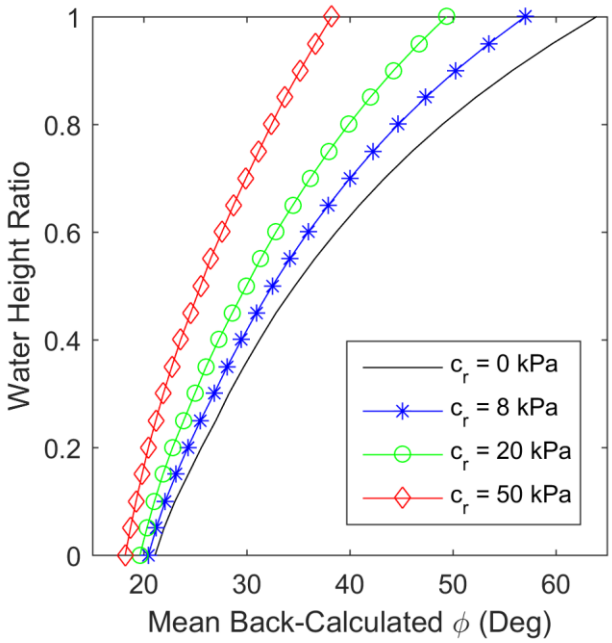

Figure 4. Mean back-calculated friction angle for changing values of water height ratio and root cohesion.

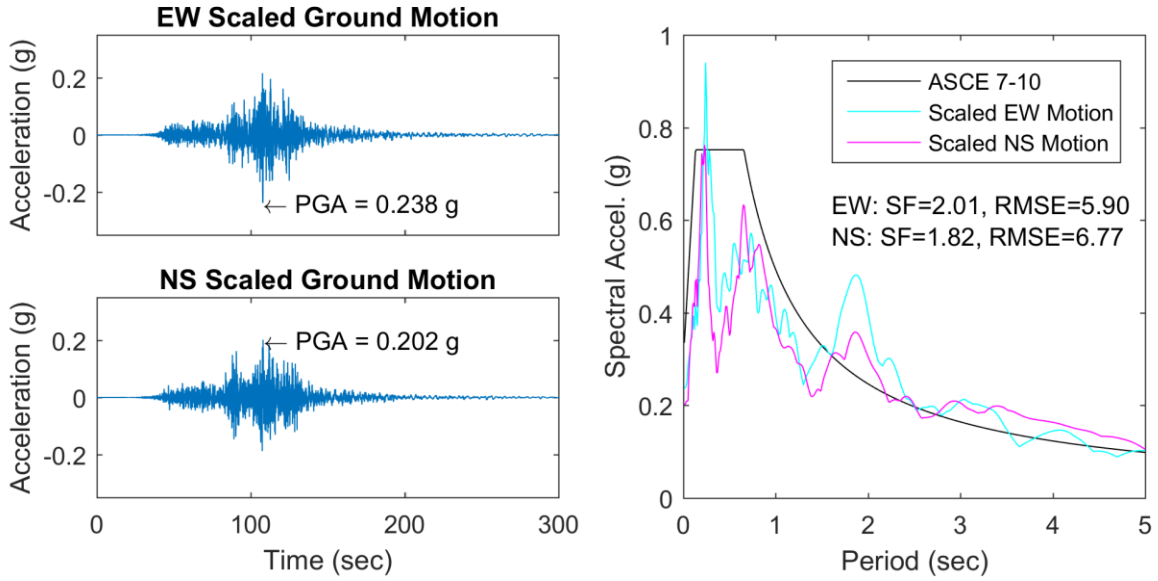

Figure 5. EW and NS acceleration-time series for the full-length scaled ground motions (left) and pseudo-spectral response with the design target spectrum (right) of two selected motions used in the scaling of 46 input motions.

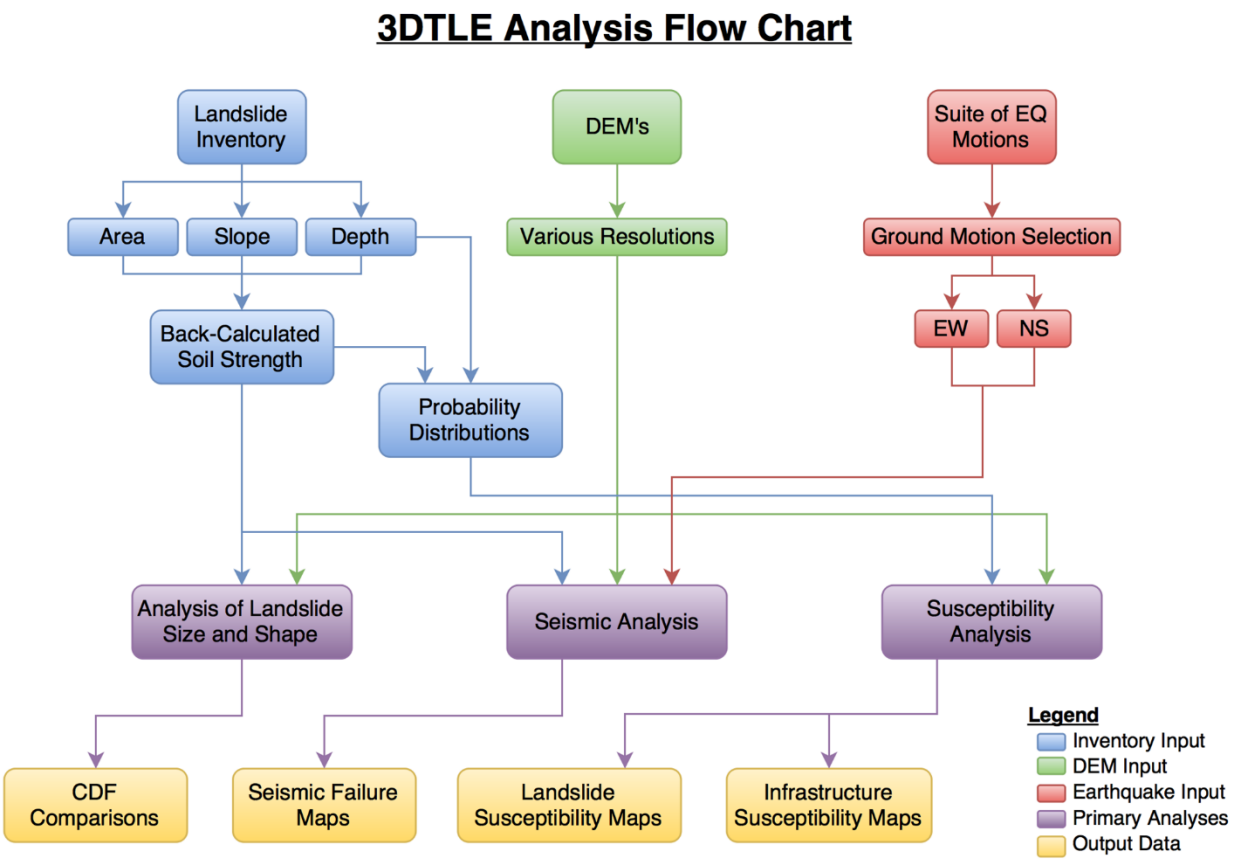

Figure 6. Flow chart of the presented framework for analyzing shallow landslides.

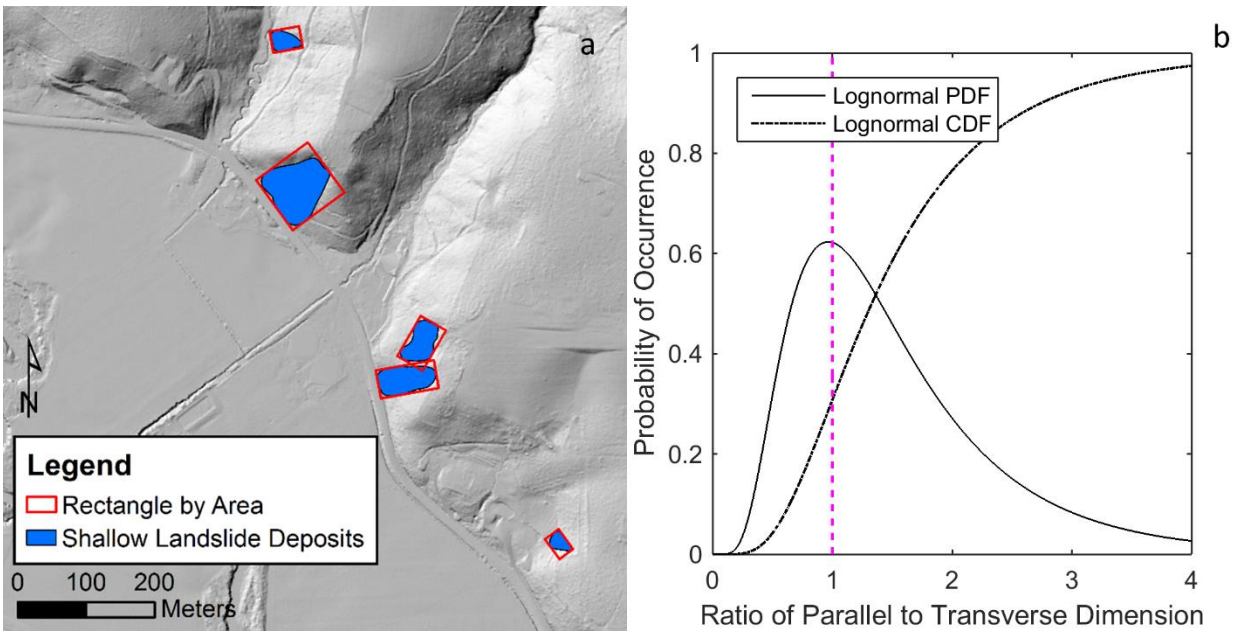

Figure 7. Analysis of landslide shape. (a) An example of fitting rectangles to landslide deposit polygons, and (b) the ratio of rectangular dimensions are depicted as probabilities of occurrence.

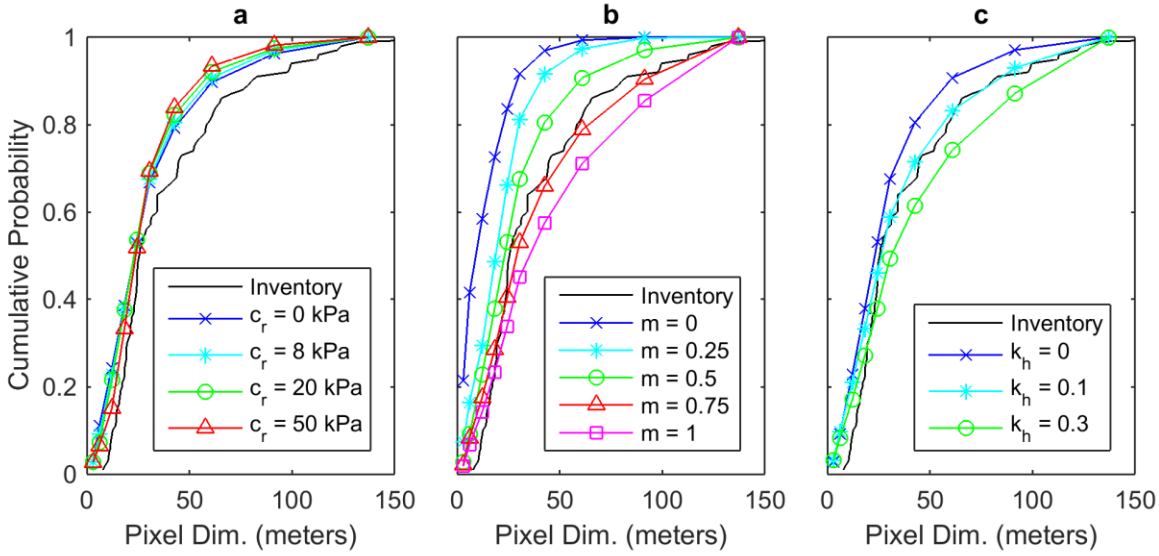

Figure 8. The dependence of failure on pixel size for changing values of (a) root cohesion, (b) water height ratio, and (c) horizontal seismic coefficient. Baseline conditions used for non-changing parameters.

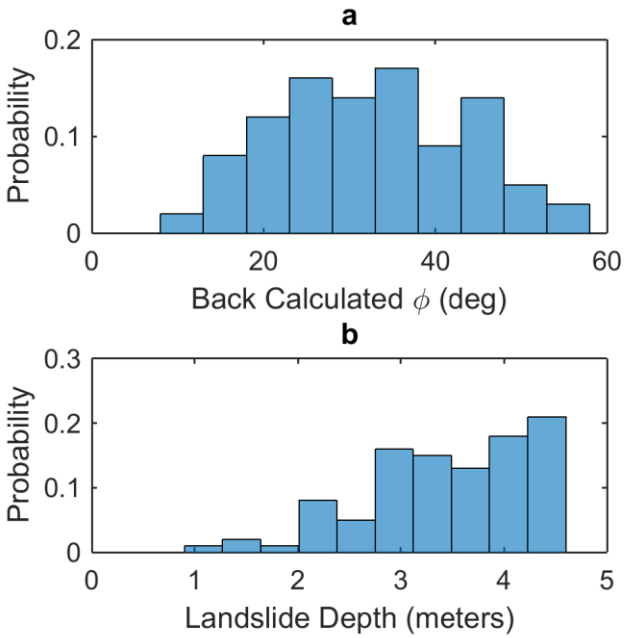

Figure 9. Distributions of (a) back-calculated friction angles for baseline conditions and (b) landslide depths obtained from the shallow landslide inventory.

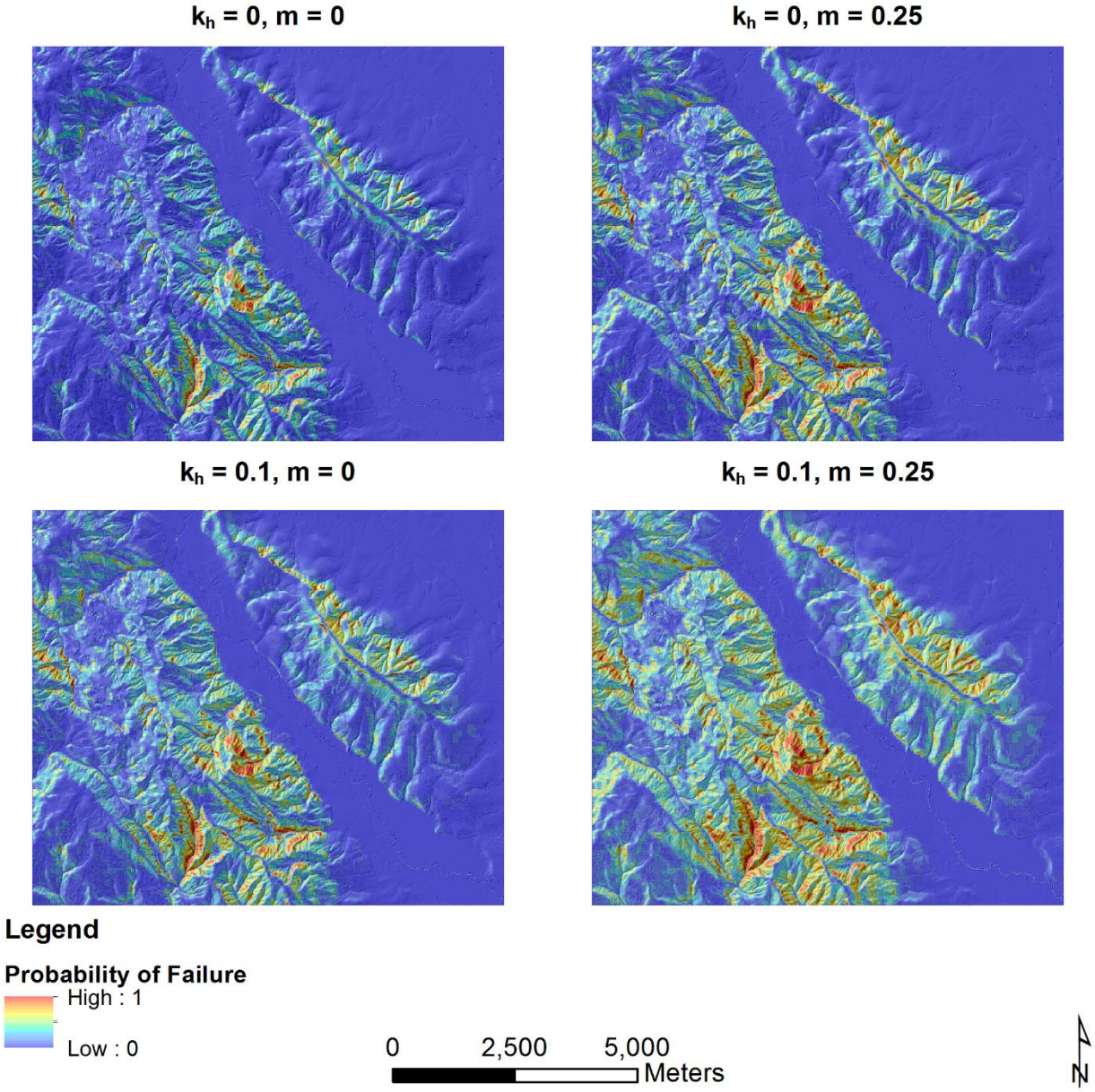

Figure 10. Landslide susceptibility maps of Gales Creek, OR calculated using a product distribution and various input values of horizontal seismic coefficient and water height ratio. Root cohesion was held constant at 0 kPa for all four maps.

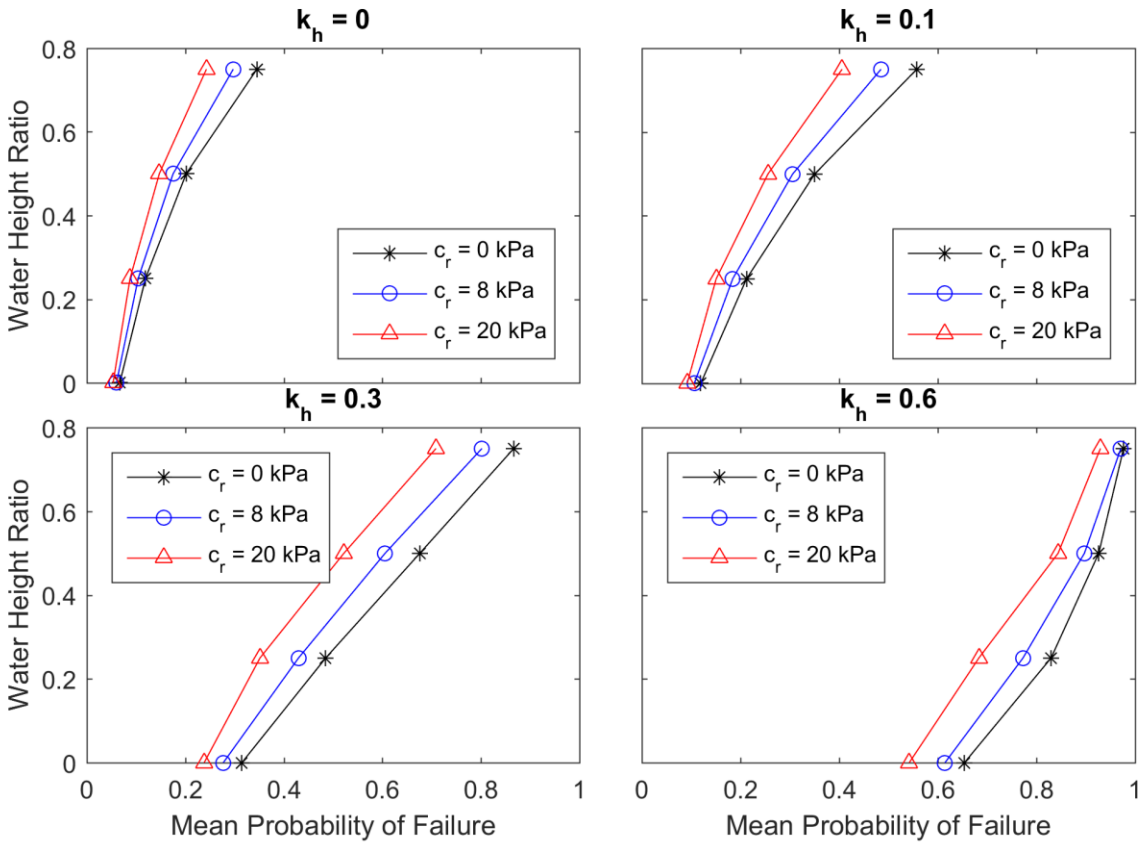

Figure 11. Comparison of the mean probability of failure calculated for various input values of horizontal seismic coefficient, water height ratio, and root cohesion.

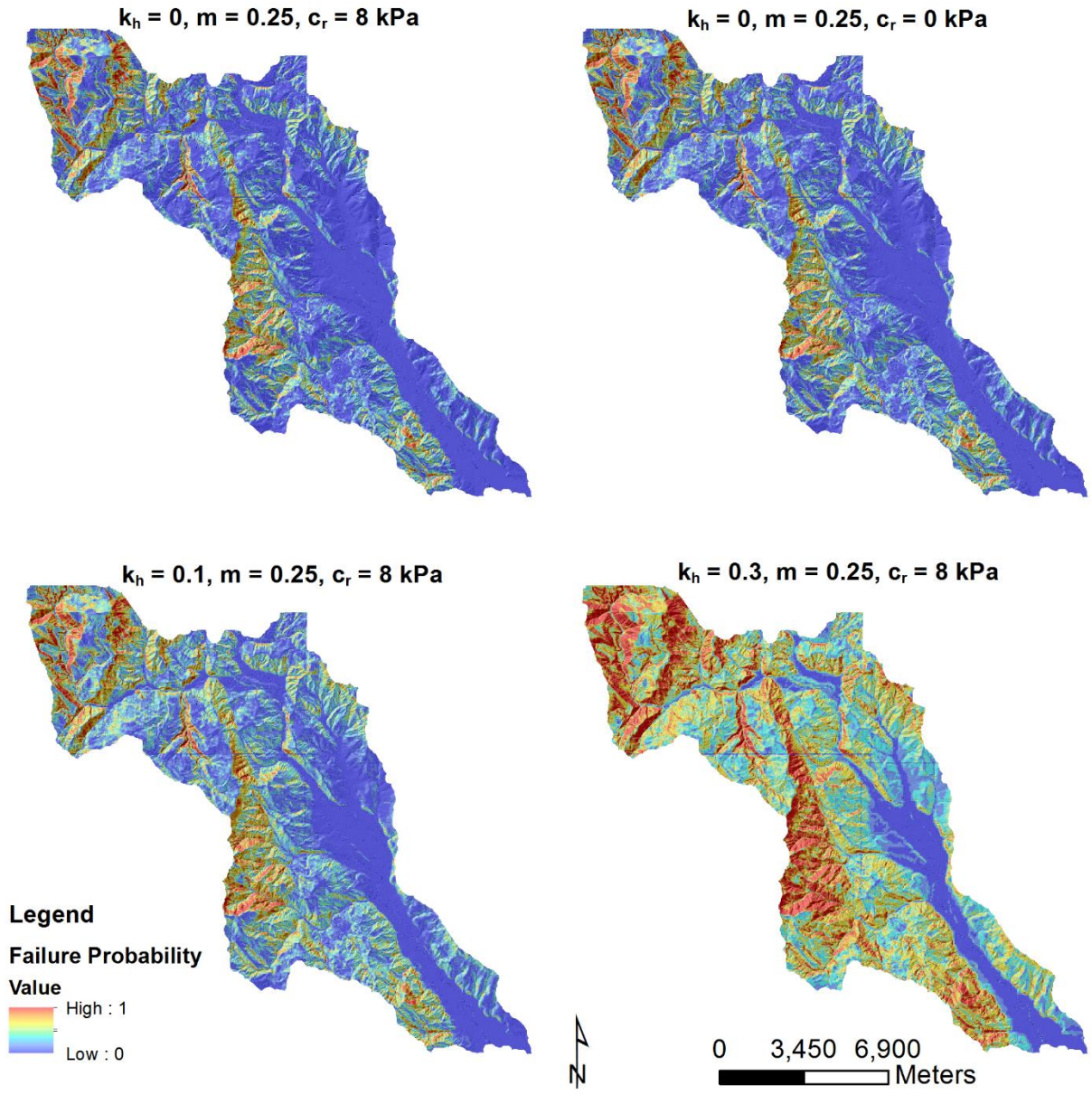

Figure 12. Susceptibility map for Gales Creek watershed showing the probability of failure for four cases of horizontal seismic coefficient, water height ratio, and root cohesion overlaid on shaded relief.

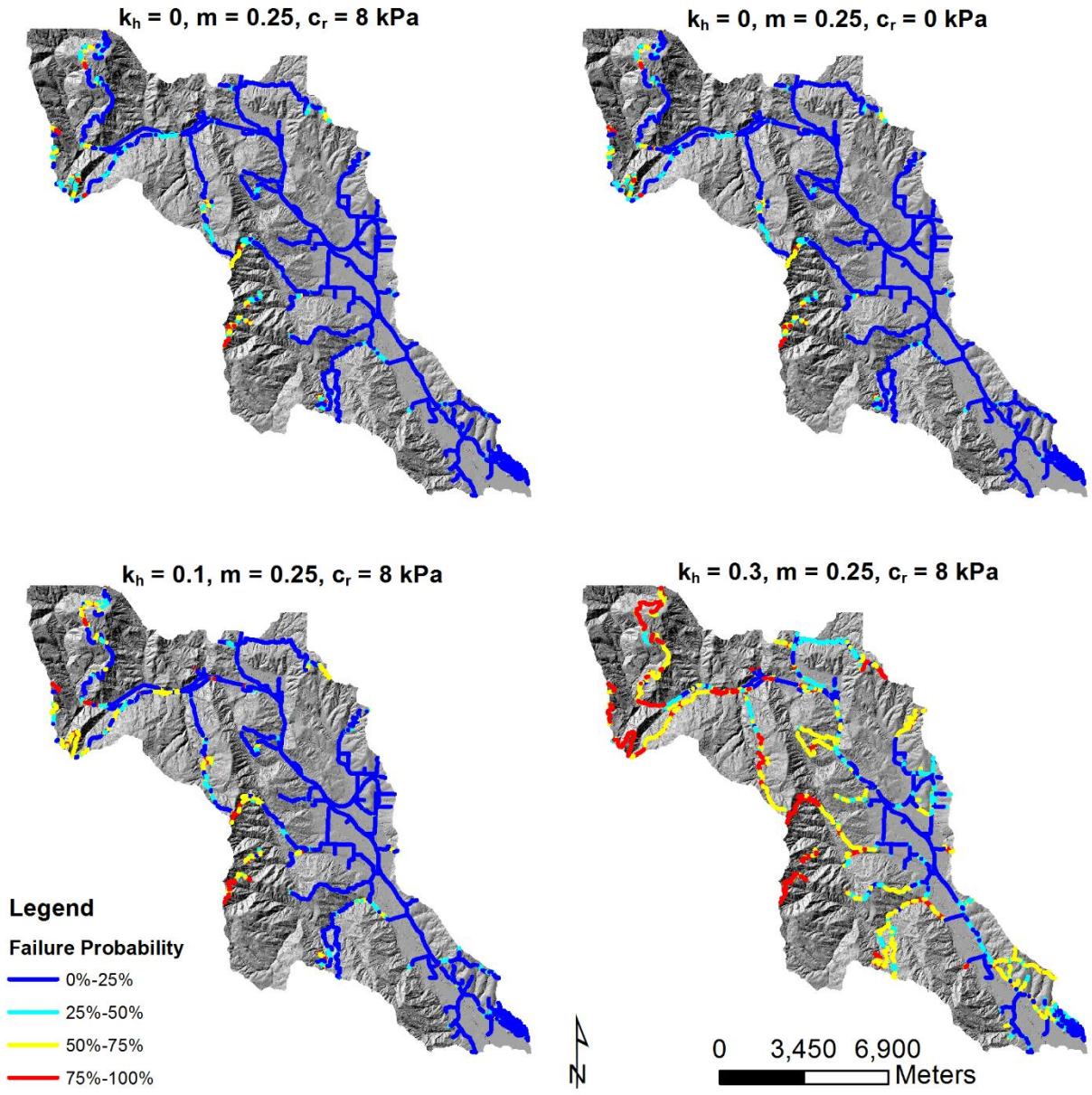

Figure 13. Infrastructure risk maps for various cases of horizontal seismic coefficient, water height ratio, and root cohesion overlaid on shaded relief maps within the Gales Creek watershed.

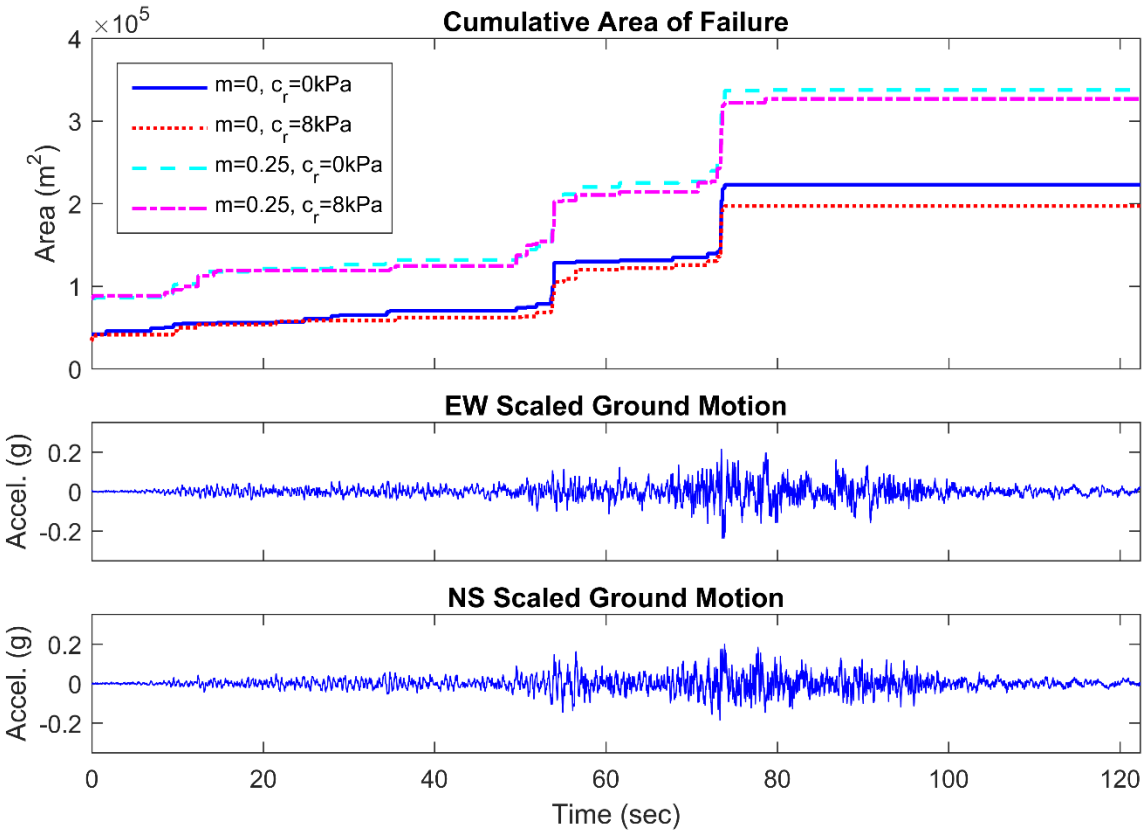

Figure 14. Cumulative area of failure obtained by applying the shorter length motions to a smaller DEM tile near Gales Creek, OR. Four different combination of water height ratio and root cohesion were analyzed.

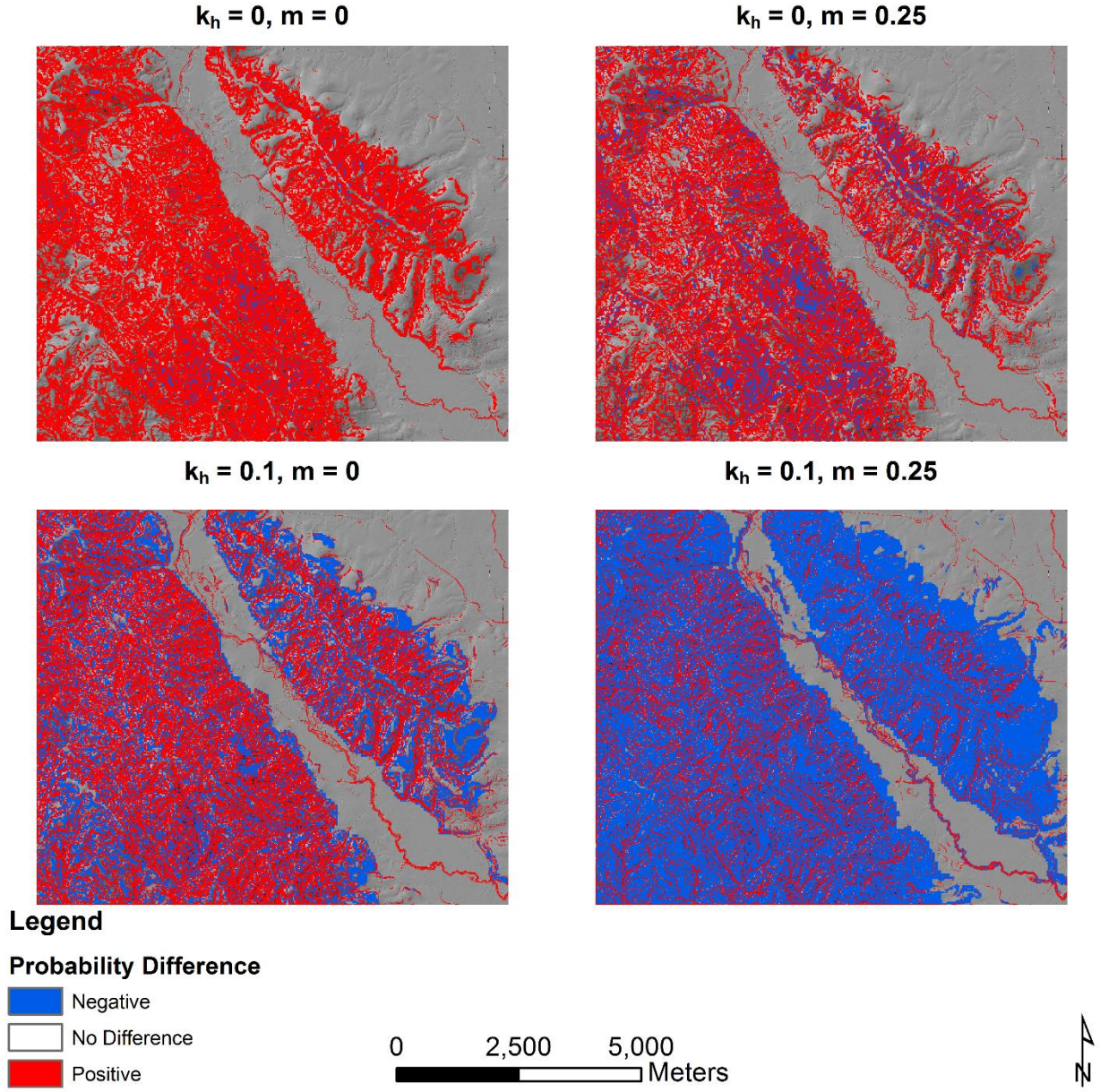

Figure 15. Difference in failure probability between the infinite slope model and the 3DTLE model for several cases. A positive difference signifies that the infinite slope model calculated a higher probability of failure, while a negative difference means 3DTLE.

Tables

Intensity Measure	EW	NS
PGA (g)	0.238	0.202
PGV (cm/sec)	42.6	44.7
PGD (cm)	17.3	23.1
I_a (m/sec)	2.31	2.29
T_m (sec)	0.912	0.825
$D_{5\text{-}95}$ (sec)	74.0	69.0

Table 1. Ground motion intensity measures for selected EW and NS scaled records. Values calculated with SeismoSignal software include peak ground acceleration, velocity, and displacement, Arias intensity, mean period, and significant duration.

Concluding Remarks

In this thesis, a framework for determining shallow landslide susceptibility was described. The 3DTLE model was used in conjunction with a shallow landslide inventory, LiDAR-derived DEMs, and various geotechnical scenarios to show the spatial distribution of probability that shallow landsliding would occur. In addition to susceptibility maps, this research described the determination of infrastructure risk by assigning failure probabilities to road networks. Furthermore, the dissimilarity between the infinite slope model and the 3DTLE model showed the importance of earth pressure boundary forces, while comparison between traditional pseudo-static analysis and the application of time- and aspect-dependent seismic motions highlighted meaningful differences in those two approaches. Lastly, considerations for future refinement of this model include the improvement of the ways in which root strength, passive earth pressure, and the influence of water are characterized.

References

Arellano, D., and Stark, T. D. (2000). “Importance of three-dimensional slope stability analyses in practice.” *Geotechnical Special Publication*, 18–32.

ASCE. (2013). *Minimum Design Loads for Buildings and Other Structures*. Standards, American Society of Civil Engineers.

Ayalew, L., and Yamagishi, H. (2005). “The application of GIS-based logistic regression for landslide susceptibility mapping in the Kakuda-Yahiko Mountains, Central Japan.” *Geomorphology*, 65(1), 15–31.

Barbosa, A. R., Mason, H. B., Romney, K., and Hall, M. (2014). “SSI-Bridge: Soil-Bridge Interaction During Long-Duration Earthquake Motions.” *University of Washington, Seattle, WA, USDOT University Transportation Center for Federal Region*, 10.

Bellugi, D., Milledge, D. G., Dietrich, W. E., McKean, J. A., Perron, J. T., Sudderth, E. B., and Kazian, B. (2015). “A spectral clustering search algorithm for predicting shallow landslide size and location.” *Journal of Geophysical Research: Earth Surface*, 120(2), 300–324.

Bischetti, G. B., Chiaradia, E. A., Simonato, T., Speziali, B., Vitali, B., Vullo, P., and Zocco, A. (2005). “Root strength and root area ratio of forest species in Lombardy (Northern Italy).” *Plant and soil*, 278(1–2), 11–22.

Burns, W. J., Maidin, I. P., and Ma, L. (2008). “Statewide Landslide Information Database for Oregon (SLIDO), Release 1.” *2008 Joint Meeting of The Geological Society of America, Soil Science Society of America, American Society of Agronomy, Crop Science Society of America, Gulf Coast Association of Geological Societies with the Gulf Coast Section of SEPM*.

Carey, T. J. (2014). “Multi-hazard framework and analysis of soil-bridge systems : long duration earthquake and tsunami loading.”

Carrara, A., Cardinali, M., Detti, R., Guzzetti, F., Pasqui, V., and Reichenbach, P. (1991). “GIS techniques and statistical models in evaluating landslide hazard.” *Earth surface processes and landforms*, 16(5), 427–445.

Carrara, A., Guzzetti, F., Cardinali, M., and Reichenbach, P. (1999). “Use of GIS technology in the prediction and monitoring of landslide hazard.” *Natural hazards*, 20(2–3), 117–135.

Choudhury, D., Sitharam, T. G., and Rao, S. K. (2004). “Seismic design of earth-retaining structures and foundations.” *Current science*, 87(10).

Cruden, D. M., and Varnes, D. J. (1996). “Landslides: investigation and mitigation. Chapter 3 - Landslide types and processes.” *Transportation Research Board Special Report*, (247).

Dai, F. C., and Lee, C. F. (2002). “Landslide characteristics and slope instability modeling using GIS, Lantau Island, Hong Kong.” *Geomorphology*, 42(3), 213–228.

Dietrich, W. E., McKean, J., Bellugi, D., Perron, T., and others. (2007). “The prediction of shallow landslide location and size using a multidimensional landslide analysis in a digital terrain model.” *Proceedings of the fourth international conference on debrisflow hazards mitigation: Mechanics, prediction, and assessment (DFHM-4). Chengdu, China*, 10–13.

Dietrich, W. E., Reiss, R., Hsu, M.-L., and Montgomery, D. R. (1995). "A process-based model for colluvial soil depth and shallow landsliding using digital elevation data." *Hydrological processes*, 9(3), 383–400.

Duncan, J. M. (1996). "State of the art: limit equilibrium and finite-element analysis of slopes." *Journal of Geotechnical engineering*, 122(7), 577–596.

Gray, D. H., and Sotir, R. B. (1996). *Biotechnical and Soil Bioengineering Slope Stabilization: A Practical Guide for Erosion Control*. John Wiley & Sons.

Hadj-Hamou, T., and Kavazanjian Jr, E. (1985). "Seismic stability of gentle infinite slopes." *Journal of Geotechnical Engineering*, 111(6), 681–697.

Hervás, J., and Bobrowsky, P. (2009). "Mapping: Inventories, Susceptibility, Hazard and Risk." *Landslides – Disaster Risk Reduction*, K. Sassa and P. Canuti, eds., Springer Berlin Heidelberg, 321–349.

Iida, T. (2004). "Theoretical research on the relationship between return period of rainfall and shallow landslides." *Hydrological Processes*, 18(4), 739–756.

Jaky, J. (1944). "The coefficient of earth pressure at rest." *Journal of the Society of Hungarian Architects and Engineers*, 78(22), 355–358.

Kottke, A., and Rathje, E. M. (2008). "A semi-automated procedure for selecting and scaling recorded earthquake motions for dynamic analysis." *Earthquake Spectra*, 24(4), 911–932.

Kramer, S. L. (1996). *Geotechnical earthquake engineering*. Prentice Hall Upper Saddle River, NJ.

Mahalingam, R., and Olsen, M. J. (2015). "Evaluation of the influence of source and spatial resolution of DEMs on derivative products used in landslide mapping." *Geomatics, Natural Hazards and Risk*, 1–21.

Milledge, D. G., Bellugi, D., McKean, J. A., Densmore, A. L., and Dietrich, W. E. (2014). "A multidimensional stability model for predicting shallow landslide size and shape across landscapes." *Journal of Geophysical Research: Earth Surface*, 119(11), 2481–2504.

Milledge, D. G., Griffiths, D. V., Lane, S. N., and Warburton, J. (2012). "Limits on the validity of infinite length assumptions for modelling shallow landslides." *Earth Surface Processes and Landforms*, 37(11), 1158–1166.

Miller, D. J., and Sias, J. (1998). "Deciphering large landslides: linking hydrological, groundwater and slope stability models through GIS." *Hydrological Processes*, 12(6), 923–941.

Ohlmacher, G. C., and Davis, J. C. (2003). "Using multiple logistic regression and GIS technology to predict landslide hazard in northeast Kansas, USA." *Engineering Geology*, 69(3), 331–343.

Oregon Geographic Information Services Unit. (2014). "Oregon Transportation Network." State of Oregon, Salem, OR.

Roering, J. J., Schmidt, K. M., Stock, J. D., Dietrich, W. E., and Montgomery, D. R. (2003). "Shallow landsliding, root reinforcement, and the spatial distribution of trees in the Oregon Coast Range." *Canadian Geotechnical Journal*, 40(2), 237–253.

Sakals, M. E., and Sidle, R. C. (2004). "A spatial and temporal model of root cohesion in forest soils." *Canadian Journal of Forest Research*, 34(4), 950–958.

Schmidt, K. M., Roering, J. J., Stock, J. D., Dietrich, W. E., Montgomery, D. R., and Schaub, T. (2001). "The variability of root cohesion as an influence on shallow landslide susceptibility in the Oregon Coast Range." *Canadian Geotechnical Journal*, 38(5), 995–1024.

Schuster, R. L. (1996). "Socioeconomic significance of landslides." *Landslides: Investigation and Mitigation. Washington (DC): National Academy Press. Transportation Research Board Special Report*, 247, 12–35.

Schwarz, M., Lehmann, P., and Or, D. (2010). "Quantifying lateral root reinforcement in steep slopes–from a bundle of roots to tree stands." *Earth Surface Processes and Landforms*, 35(3), 354–367.

Shukla, S. K. (2013). "Generalized analytical expression for dynamic passive earth pressure from c–φ soil backfills." *International Journal of Geotechnical Engineering*, 7(4), 443–446.

Shukla, S. K. (2015). "Generalized analytical expression for dynamic active thrust from c–φ soil backfills." *International Journal of Geotechnical Engineering*, 9(4), 416–421.

Tsai, T.-L., and Yang, J.-C. (2006). "Modeling of rainfall-triggered shallow landslide." *Environmental Geology*, 50(4), 525–534.

Waldron, L. J. (1977). "The shear resistance of root-permeated homogeneous and stratified soil." *Soil Science Society of America Journal*, 41(5), 843–849.

Westen, C. van, and Terlien, M. J. T. (1996). "An approach towards deterministic landslide hazard analysis in GIS. A case study from Manizales (Colombia)." *Earth Surface Processes and Landforms*, 21(9), 853–868.

Wu, T. H., McKinnell III, W. P., and Swanston, D. N. (1979). "Strength of tree roots and landslides on Prince of Wales Island, Alaska." *Canadian Geotechnical Journal*, 16(1), 19–33.

Wu, W., and Sidle, R. C. (1995). "A distributed slope stability model for steep forested basins." *Water resources research*, 31(8), 2097–2110.

Xie, M., Esaki, T., and Cai, M. (2006). "GIS-based implementation of three-dimensional limit equilibrium approach of slope stability." *Journal of geotechnical and geoenvironmental engineering*, 132(5), 656–660.

Xu, C., Xu, X., Yao, Q., and Wang, Y. (2013). "GIS-based bivariate statistical modelling for earthquake-triggered landslides susceptibility mapping related to the 2008 Wenchuan earthquake, China." *Quarterly journal of engineering geology and hydrogeology*, 46(2), 221–236.